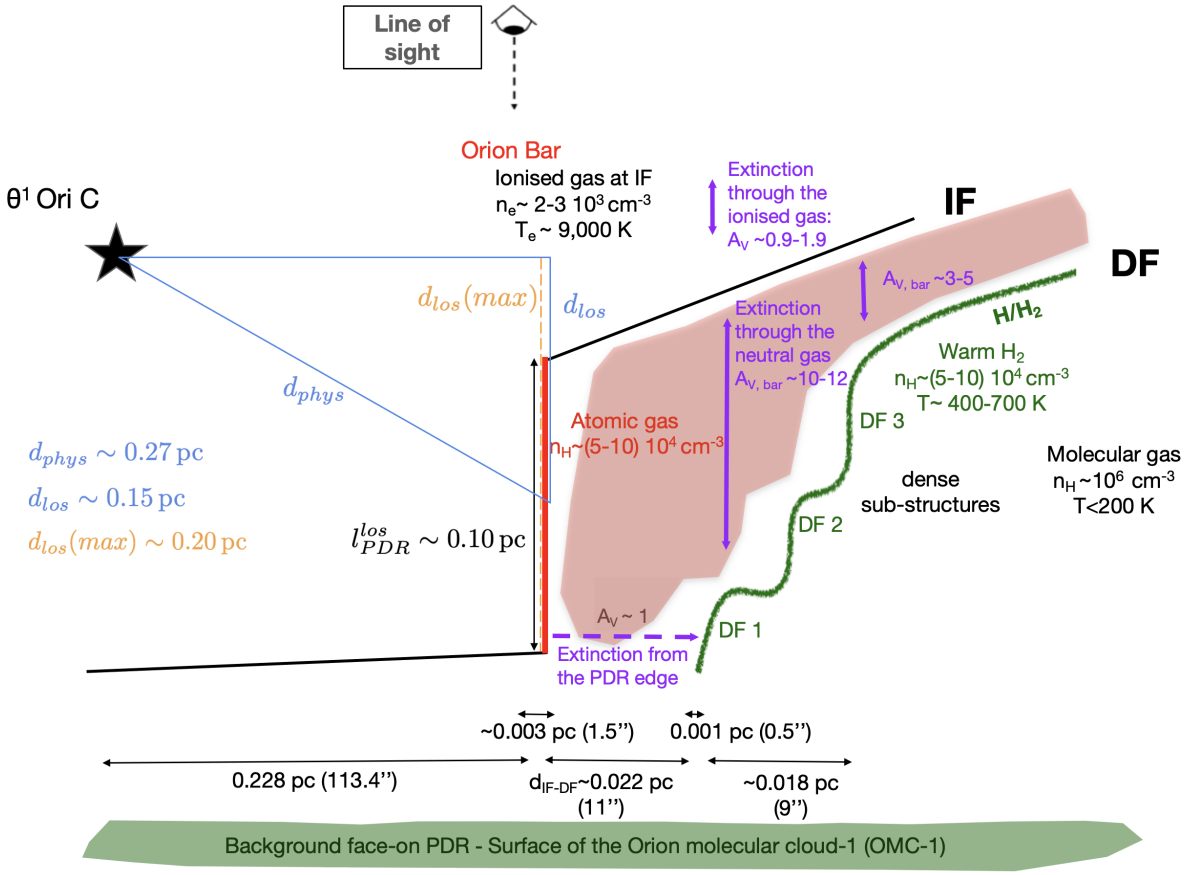


Fig. 14. Schematic overview of the Bar as inferred from JWST and other observations (e.g. Jansen et al. 1995; Wen & O'dell 1995; O'Dell 2001; Pellegrini et al. 2009). It shows the main features discussed in this paper and Habart et al. (2024, based on NIRCam and MIRI imaging). Given the complexity of the PDR surface, parameters derived in this paper are specific for the NIRSpec mosaic. We note that for clarity, the dimensions perpendicular to the bar are not to scale; the true spatial scales are explicitly given in the annotations. In addition, the sketch does not include foreground material, that includes a layer of ionised gas O'Dell et al. (2020) and, closer to the observer, layers that are grouped together under the designation as the Veil (e.g. Rubin et al. 2011; Boersma et al. 2012; van der Werf et al. 2013; Pabst et al. 2019, 2020).

(Del Zanna & Storey 2022) may necessitate a new analysis of the [He$^+$]/[H$^+$] abundance ratio to take full advantage of the high quality of the NIRSpec data.

We furthermore confirm the observed He I 2.058/1.70 ratio as detected by Marconi et al. (1998). This ratio ranges between about 7–10 (Fig. 12). These authors argue that one can compare this ratio with the model predictions of Smits (1996), as the He I 1.70 μm transition arises from the same upper level as the 4471 Å transition used for normalisation in the model calculations. The observed value is significantly enhanced with respect to the model prediction, which Marconi et al. (1998) potentially attributes to the neglect of collisional effects and line trapping.

Lastly, we can obtain an estimate of the electron temperature, T_e, from the He I line ratios 2.1649/2.1137 and 2.1649/2.118 based on the diagnostic diagram of Martín-Hernández et al. (2003, their Fig. 7b). We find an electron temperature, T_e, of about 9000–9500 K and an optical depth of the 2^3S metatstable level, τ_{3890}, of ~0 for each of the template spectra except for DF 1 for which we find an electron temperature, T_e, of about 8000 K.

6.3. OI and NI fluorescent emission

6.3.1. Spatial and spectral characteristics

The fluorescent lines of O I at 1.129 and 1.317 μm arise from the partially neutral gas in the ionisation front from UV-pumping by 1027 and 1040 Å photons, respectively, followed by radiative decay. In addition, there are multiple indirect routes to pumping the upper levels of these lines. For example, Henney (2021) reported that roughly half of the pumping of the O I 8446 Å fluorescence line arises from more excited levels. Hence, a detailed investigation is warranted to assess the relative importance of the various pumping routes. Assuming solely pumping by the strongest UV resonance lines, similar intensities are expected for both IR transitions. Yet, the O I 1.317 μm intensity is, on average, about 3 times the O I 1.129 μm intensity in the IF and the filamentary structure in the atomic PDRs (i.e. where the O I 1.317 μm intensity >15σ). This is in contrast with previous results. Indeed, Marconi et al. (1998) reported that the 1.129 μm line is 1) equal in strength to the 1.317 μm line at two positions – from which they concluded that pumping of the upper level of the 1.129 μm transition by resonantly scattered Lyman β photons (1026 Å) is negligible – and 2) stronger than the 1.317 μm line at one position, which we do not see anywhere in the NIRSpec mosaic. Likewise, Walmsley et al. (2000) observed similar 1.129 and 1.317 μm line intensities at two positions, while a third position exhibited a stronger 1.317 μm intensity, albeit with a lower factor than observed in the NIRSpec data (1.317/1.129 ~ 1.4). As these observations probe different positions of a highly structured PDR, seeing variations across the Bar is perhaps not that surprising. However, the origin of the enhanced O I 1.317/1.129

Table 2. Parameters employed or derived for the Orion Bar.

Parameter	Value	Reference
Distance	414 ± 7 pc [(a)]	Menten et al. (2007)
	1″= 0.002 pc	
Projected distance, $d_{\rm proj}$, between θ^1 Ori C and the IF [(b)]	0.228 pc	Sect. 5.1
Physical distance, $d_{\rm phys}$, between θ^1 Ori C and the IF	~0.27 pc	Sect. 6.3.2
Transverse size $l^{\rm los}_{\rm PDR}$	~0.10 pc	Sect. 6.3.2
Line-of-sight distance, $d_{\rm los}$, between θ^1 Ori C and the IF		Sect. 6.3.2
Average	~0.15 pc	
Minimum	~0.05 pc	
Maximum	~0.20 pc	
Projected distance between He-IF and H-IF [(c)]	0.5×10^{-2} pc; 2.5″	Sect. 6.2
Projected distance between IF and DF d_{IF-DF} [(c,d)]	$(2.2, 2.9, 4.0) \times 10^{-2}$ pc	Sect. 5.1
	11.0″, 14.5″, 19.8″	
G_0 at IF	$\sim(2.2–7.1) \times 10^4$	Sect. 6.3.2, Appendix F
Width IF at peak G_0	$(0.22–0.34) \times 10^{-2}$ pc	Sects. 5.1, 6.3
	1.1″ – 1.7″	
Condition for face-on PDR to dominate G_0	$d_{\rm proj} \geq 0.24$ pc	Sect. 6.3.1
FUV dust cross-section σ_H	6.5×10^{-22} cm^2 / H	Cardelli et al. (1989); Blagrave et al. (2007) Schirmer et al. (2022)
$R_V = A_V/E(B-V)$	5.5	Cardelli et al. (1989); Blagrave et al. (2007)
A_V/N_H	3.5×10^{-22} mag/cm^{-2}	Cardelli et al. (1989); Blagrave et al. (2007)
Total IR emission $L_{\rm IR}$	9.5×10^3 L$_\odot$	Salgado et al. (2016)
Foreground extinction A_V	0.9–1.9 mag	Sect. 6.1
Emission measure EM (Brγ)	$(0.84–4.15) \times 10^6$ pc cm^{-6}	Sect. 6.1
Rms electron density $n_{e,\rm rms}$ near IF (Brγ)	~9000 cm^{-3}	Sect. 6.1
Density at the IF n_e [(d)]	$2–3 \times 10^3$ cm^{-3}	Weilbacher et al. (2015)
Temperature at the IF T$_e$ [(d)]	$\sim 9 \times 10^3$ K	Weilbacher et al. (2015)
Density in atomic PDR n_H (AIB emission) [(d)]	$(5–10) \times 10^4$ cm^{-3}	Habart et al. (2024, Sect. 5.1)
Density from NIR H_2 n_H	$(3.5) \times 10^4$ to 10^5 cm^{-3}	Sect. 6.4
Temperature at the DF T	~400–700 K	Van De Putte et al. (2024) Allers et al. (2005)
Emission measure EM ([C I] 0.984 μm)	$(1.1–2.8) \times 10^5$ pc cm^{-6}	Sect. 6.5

Notes. [(a)]See Habart et al. (2024) for a discussion on the adopted distance. [(b)]IF is defined by the peak emission of the [O I] 6300 Å and [Fe II] 1.644 μm emission. [(c)]Projected distance along the NIRSpec cut. As the cut is not perpendicular to the IF, a correction factor of cos(19.58°)=0.942 needs to be applied to obtain a perpendicular distance from the IF. [(d)]Given the complexity of the PDR surface, parameters given are specific for the NIRSpec FOV. For average values across the entire Bar, see Habart et al. (2024).

ratio observed here and in one position of Walmsley et al. (2000) is unclear and requires further investigation.

The observed O I 1.317 μm intensity decreases with distance from the ionisation front (Figs. 7 and 9). The location of the cut, crossing both the primary and secondary ridge, results in a very sharp, double-peaked profile just beyond the ionisation front. In addition, its radial profile shows multiple peaks between 0.34 and 1.07×10^{-2} pc from the IF (between 1.7″ and 5.3″), followed by a slow drop at larger distances. We note that the observed O I 1.317 μm intensity follows the [O I] 6300 Å intensity to some degree (Fig. 9). The ionisation front has a typical H I column density of 6×10^{18} cm^{-2} (Tielens 2005, Eq. (7.25)), corresponding to an optical depth in the O I UV pumping lines of ~30 (Marconi et al. 1998). Hence, the strongest UV resonance lines that pump the O I near-IR lines (i.e. 1027 and 1040 Å photons for respectively the 1.129 and 1.317 μm lines) are on the logarithmic part of the curve of growth in the PDR itself. We note that indirect pumping of these lines may involve weaker UV lines in different parts of the curve of growth. We attribute the multiple peaks to the presence of undulations in the Bar surface. The subtle differences in the intensity distribution of the O I 1.317 μm line and the [O I] 6300 Å line may reflect local acceleration zones of the gas in the ionisation front that Doppler shift unattenuated stellar photons into the UV pumping wavelengths of O I 1.317 μm ([O I] 6300 Å emission is due to collisional excitation). We note that for an intrinsic line width of 3 km s^{-1}, an acceleration by 1 km/s will increase the UV pumping photon flux by 30%. In addition, this area is known to host many collimated velocity flows (such as HH203, 204, and 528, e.g. Méndez-Delgado et al. 2021). Some of the observed difference may be related to these flows. We attribute the gradual decrease in both the O I 1.317 μm and the [O I] 6300 Å intensity beyond 1.07×10^{-2} pc from the IF (5.3″; Fig. 9) to the change over from an edge-on to a face-on geometry of the ionisation front, coupled with the geometric dilution of the incident UV field intensity. This transition from edge-on to face-on geometry occurs over a very small distance (~1″, 6×10^{15} cm). Lastly, we ascribe part of the prominent triangular region of enhanced O I 1.317 μm at $0.6–1.2 \times 10^{-2}$ pc (3–6″) behind the ionisation front (Fig. 8) to a local gas acceleration zone. As there is no counterpart in the [O I] 6300 Å line for the E-W filament, this acceleration must occur inside the PDR itself.

6.3.2. Bar geometry & strength of the FUV radiation at the PDR surface

It is well recognised that, on a global (10's of arcsec) scale, the Bar shows the expected stratification of an edge-on PDR with a clearly separated ionisation front, atomic region, H_2 dissociation front, and molecular zone on the sky (Tielens et al. 1993; Tauber et al. 1994; Hogerheijde et al. 1995; Bernard-Salas et al. 2012). This is well supported by these high resolution NIRSpec imaging data as well as by JWST NIRCam and MIRI imaging observations (Habart et al. 2024), Keck observations (Habart et al. 2023), and recent ALMA studies of the molecular emission (Goicoechea et al. 2016). Both this NIRSpec study (Fig. 7) and the other studies reveal that on a local (~arcsec) scale the Bar is highly structured as the FUV radiation field penetrates a clumpy PDR region. We expect that the width of the ionisation front as measured in the [O I] 6300 Å line and the near-IR O I (e.g. 1.317 μm) fluorescence lines is dominated by this small-scale structure. In the past, the observed width of these tracers has been interpreted in terms of a inclination angle of the Bar with respect to the line of sight (e.g. Marconi et al. 1998; Walmsley et al. 2000; Salgado et al. 2016) but this is really untenable given, for example, the structured appearance of the O I emission (Fig. 8), the H_2 dissociation fronts in the NIRSpec, NIRCam, and Keck maps (Fig. 7, Habart et al. 2023, 2024), and the ALMA HCO^+ maps (Goicoechea et al. 2016). The O I data can be used to derive a strict upper limit to the inclination of ~4° (e.g. Marconi et al. 1998; Walmsley et al. 2000, see Appendix F for details) but as exemplified by the NIRSpec maps (Fig. 7), there is no large-scale curvature associated with the Bar and it is essentially an edge-on, limb-brightened PDR.

We can use the obtained values for the optical depth at 100 μm from Salgado et al. (2016) to derive the geometry of the Bar. These authors observed the SED of the dust emission in the Bar over its entire wavelength range and were able to fit this SED with two modified blackbodies assuming optical thin emission. The Bar is very pronounced in the optical depth map of the warm component, τ_{warm}, with $\tau_{warm} \sim 1 \times 10^{-2}$ (Fig. 8 in Salgado et al. 2016). With the ratio of the extinction at 100 μm to the Hydrogen column density, A_{100}/N_H, being equal to 6.2×10^{-25} magn cm^{-2} H – atom^{-1} for an R_V of 5.5 (Draine 2011), we obtain $N_H = 1.75 \times 10^{22}$ H – atoms cm^{-2} which results in estimate of the transverse size of l^{los}_{PDR} of 0.10 pc for a density, n_H, of 5×10^4 cm^{-3}. This is consistent with model predictions of the Bar geometry (e.g. Tielens et al. 1993; Pellegrini et al. 2009). Using the observed size of the Bar (0.32 pc), the obtained transverse size of l^{los}_{PDR} then provides an estimate of the absorbing area A_{abs} of 0.033 pc^2 assuming a rectangular absorbing area. The obtained absorbing area then in turn provides an estimate of the physical distance between θ^1 Ori C and the IF, d_{phys}, for a given stellar luminosity from $A_{abs} = L_{IR}/(L_\star/(4\pi d^2_{phys}))$ as the total IR emission is a measure for the amount of stellar radiation absorbed by the Bar (e.g. Salgado et al. 2016). We adopt the higher stellar FUV luminosity of 2.7×10^5 L$_\odot$ employed by Salgado et al. (2016), as the lower stellar FUV luminosity does not provide physical results[22]. We obtain a physical distance between the θ^1 Ori C and the IF, d_{phys}, of 0.27 pc. Given the physical size of the IF, we assume this distance reflects the physical distance from the mid-point of the IF to θ^1 Ori C (Fig. 14). Given a projected distance between θ^1 Ori C and the IF, d_{proj}, of 0.228 pc, this constraints the distance between θ^1 Ori C and the mid-point of the IF projected along the line of sight, d_{los}, to 0.15 pc (Fig. 14). Consequently, θ^1 Ori C is located at a distance of 0.10 pc in front of the start of the IF along the line of sight and the depth of the Bar (end-point) from θ^1 Ori C along the line of sight is 0.20 pc (Fig. 14).

Finally, we can use the obtained values for the absorbing area, A_{abs}, to derive the strength of the FUV radiation field, G_0, following Salgado et al. (2016, Sect. 4.1). These authors equate the observed total IR emission to the product of the strength of the FUV radiation field, G_0, and the area at the surface of the PDR absorbing stellar radiation, A_{abs}. Employing the total IR emission reported by these authors, this results in a G_0 of 7.1×10^4. This value is consistent with Tielens & Hollenbach (1985b), who derived G_0 from an analysis of the [O I] and [C II] atomic fine-structure lines observed towards the Bar PDR, and slightly higher than the G_0 of 2.6×10^4 reported by Marconi et al. (1998), who derived G_0 based on their observations of the near-IR O I fluorescent lines. We further note that this G_0 is consistent with values derived from the NIRSpec O I 1.317 μm line assuming that the Bar is inclined at a 4° angle (see Appendix F).

6.4. Rotationally and vibrationally excited H_2 emission

H_2 emission is observed throughout the mosaic (see Fig. 7). We detect a large number of ro-vibrational lines in our data. For a detailed inventory of the observed H_2 lines and the spatial distribution of their emission, we refer the reader to Sect. 4.1 and Appendix B, and Sect. 5.1, respectively. We report the measured fluxes for selected H_2 lines detected in the five templates in Table 3. We note that the H_2 line intensity is strongest in DF 3, followed by DF 2, DF 1, atomic PDR, and H II region. This variation in intensity is also observed in the surface brightness line cut across the NIRSpec mosaic presented in Fig. 9. Moreover, there is an increase in H_2 emission at the position of the two proplyds. The in-depth analysis of the H_2 emission in proplyd 203–506 is discussed in Berné et al. (2024). Here, we focus on the H_2 emission observed in the five templates. We highlight that the H_2 emission observed in the H II region originates from the background face-on PDR in OMC-1 (see Fig. 14). The emission from this background face-on PDR was previously observed with Herschel in other PDR tracers, particularly in high-J CO, CH^+ lines (Parikka et al. 2018) and [O I] 63 and 145 μm and [C II] 158 μm (Bernard-Salas et al. 2012), as well as, with *Spitzer* in AIB emission (Knight et al. 2022). In contrast, the H_2 emission observed in the atomic PDR and the three dissociation fronts originates from the edge-on PDR in the Bar itself.

The H_2 lines are powerful tools to probe the physical conditions of the emitting region. We use the observed lines to probe the extinction within the PDR and density throughout the mosaic. While we estimate the foreground visual extinction, A_V, using the H I recombination lines (Sect. 6.1), we use the H_2 lines to measure the extinction in the neutral H I region of the bar using the foreground and intermingled formalisms, referred to as $A_{V_{bar}}$ and $A_{V_{bar},I}$ respectively. The foreground formalism assumes that the dust is in front of the region emitting H_2, whereas the intermingled formalism assumes that the dust is mixed with the gas emitting H_2. Comparison of the ratio of lines that arise from the same upper v and J state with the corresponding intrinsic flux ratio gives a measure of amount of extinction within the PDR ($A_{V_{bar}}$ and $A_{V_{bar},I}$). We use the ratio of the H_2 lines 1–0 S(1) and 1–0 O(5), which originates from the same upper level, corrected

[22] The physical distance is smaller than the projected distance when adopting the lower stellar FUV luminosity.

Table 3. Excerpt of intensities (observed and corrected for extinction using foreground and intermingled formalisms) and column densities of selected H_2 lines in v=0 and v=1 states as observed in the five templates.

Template	Line	Wavelength	Observed intensity	Extinction corrected intensity		Column density	
		(μm)	($\times10^{-5}$ erg cm^{-2} s^{-1} sr^{-1})			($\times10^{15}$ cm^{-2})	
				Foreground	Intermingled	Foreground	Intermingled
H II region	0–0 S(8)	5.0531152	$2.570^{2.649}_{2.491}$	$2.770^{2.855}_{2.685}$	–	$2.736^{2.820}_{2.652}$	–
H II region	0–0 S(9)	4.6946139	$6.290^{6.407}_{6.173}$	$6.816^{6.943}_{6.689}$	–	$4.131^{4.208}_{4.054}$	–
H II region	0–0 S(10)	4.4097910	$1.310^{1.378}_{1.242}$	$1.427^{1.502}_{1.353}$	–	$0.567^{0.596}_{0.537}$	–
H II region	0–0 S(11)	4.1810772	$3.350^{3.500}_{3.200}$	$3.670^{3.834}_{3.506}$	–	$1.008^{1.053}_{0.963}$	–

Notes. The complete table is available at the CDS.

Table 4. Column densities and excitation temperatures obtained from fitting the excitation diagrams of the H_2 lines observed towards the H II region, the atomic PDR, DF 1, DF 2, and DF 3 (Fig. 15).

	Foreground formalism		Intermingled formalism	
H_2 series	N_{H_2} ($\times10^{18}$ cm^{-2})	T (K)	N_{H_2} ($\times10^{18}$ cm^{-2})	T (K)
		H II region		
0–0 S	0.19 ± 0.05	2753 ± 172	–	–
1–0 Q	0.24 ± 0.14	2391 ± 376	–	–
1–0 O	3.59 ± 6.45	1135 ± 335	–	–
1–0 S	0.40 ± 0.10	2034 ± 107	–	–
1–1 S	0.08 ± 0.03	3813 ± 223	–	–
		Atomic PDR		
0–0 S	0.12 ± 0.04	3393 ± 224	0.12 ± 0.05	3396 ± 224
1–0 Q	0.61 ± 0.35	1996 ± 284	0.62 ± 0.36	1996 ± 284
1–0 O	11.5 ± 15.7	969 ± 207	10.9 ± 16.2	967 ± 207
1–0 S	0.96 ± 0.32	1598 ± 109	0.99 ± 0.33	1592 ± 108
1–1 S	0.13 ± 0.08	3527 ± 413	0.14 ± 0.09	3531 ± 414
		DF 1		
0–0 S	0.58 ± 0.09	3033 ± 119	0.89 ± 0.15	3105 ± 121
1–0 Q	9.83 ± 2.96	1477 ± 88	17.8 ± 5.36	1481 ± 88
1–0 O	10.7 ± 11.0	1326 ± 259	22.9 ± 20.35	1273 ± 238
1–0 S	5.07 ± 3.07	1617 ± 206	10.5 ± 6.49	1534 ± 189
1–1 S	0.27 ± 0.04	3699 ± 100	0.40 ± 0.06	3795 ± 100
		DF 2		
0–0 S	0.73 ± 0.09	2996 ± 84	0.75 ± 0.10	3001 ± 84
1–0 Q	4.10 ± 2.54	1728 ± 204	4.26 ± 2.64	1728 ± 204
1–0 O	8.23 ± 8.62	1437 ± 309	8.66 ± 9.09	1432 ± 306
1–0 S	5.46 ± 2.94	1723 ± 193	5.77 ± 3.12	1712 ± 191
1–1 S	0.40 ± 0.08	3631 ± 124	0.41 ± 0.08	3638 ± 124
		DF 3		
0–0 S	0.89 ± 0.10	2852 ± 57	0.89 ± 0.10	2852 ± 57
1–0 Q	6.18 ± 5.61	1527 ± 218	6.21 ± 5.63	1527 ± 219
1–0 O	16.7 ± 27.8	1151 ± 320	16.7 ± 28.0	1151 ± 320
1–0 S	14.0 ± 12.1	1180 ± 163	14.1 ± 12.2	1179 ± 163
1–1 S	0.65 ± 0.13	3156 ± 110	0.65 ± 0.13	3157 ± 110

Notes. Except for the H II region, all the H_2 lines in the excitation diagrams are first corrected for foreground visual extinction and subsequently for extinction within the PDR using the foreground and intermingled formalisms. In the H II region, the lines are only corrected for the foreground visual extinction.

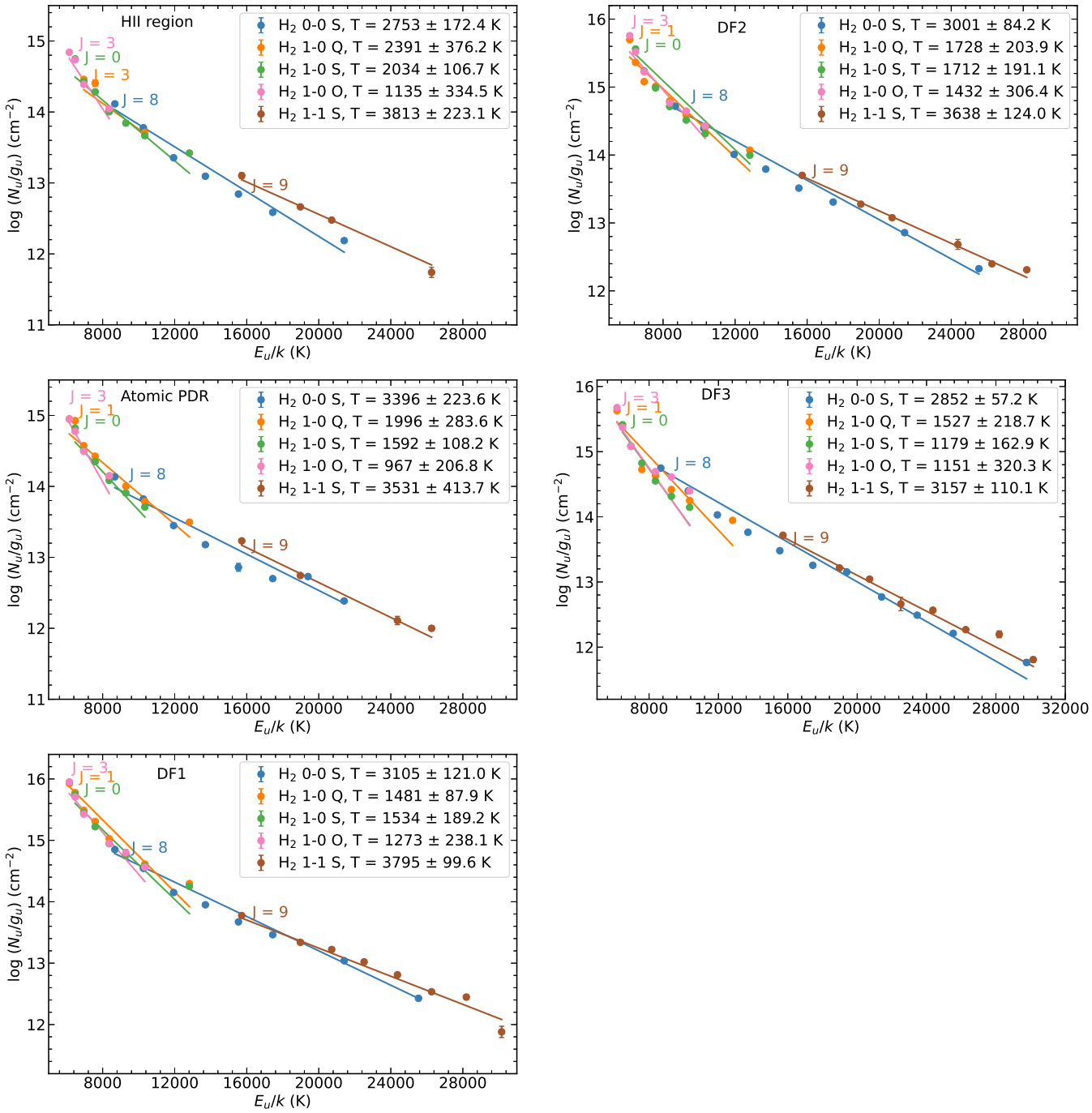


Fig. 15. Excitation diagrams of H_2 lines observed towards the H II region, atomic PDR, DF 1, DF 2, and DF 3. With the exception of H II region, the H_2 lines in the excitation diagrams are first corrected for foreground visual extinction and subsequently for extinction within the PDR using the intermingled formalism. In H II region the lines are only corrected for the foreground visual extinction. The excitation diagrams for the 0–0 S, 1–0 Q, 1–0 S, 1–0 0, and 1–1 S levels of H_2 are fitted using a single temperature component of the gas, and the individual fits are represented by solid lines. The resulting temperature and column densities obtained from the fits are listed in Table 4.

for foreground extinction, to estimate the internal PDR extinction. Table 1 shows the $A_{V_{\rm bar}}$ and $A_{V_{\rm bar},I}$ values obtained for the five templates using both the foreground and intermingled formalisms. Moreover, in Fig. 11, we present the line cut across the mosaic of $A_{V_{\rm bar}}$. We note that the internal PDR extinction is highest in the DF 1, followed by DF 2, the atomic PDR, and DF 3. In the H II region, the internal PDR extinction is ∼ 0. The high value of the internal PDR extinction in DF 1 implies that DF 1 is further along the line of sight than DF 2 and DF 3. Therefore, the column density along the line of sight increases for DF 1, which is more distant from the observer (but closer in projected distance from the ionisation front). The measured flux for the H_2 lines corrected for the foreground and internal PDR extinction in the five templates is presented in Table 3.

The H_2 line ratio of 1–0 S(1)/2–1 S(1) is sensitive to the density. We present a line cut across the mosaic of this ratio in Fig. 11. This ratio exhibits values ranging from ∼ 3–5 across the mosaic and begins to increase beyond DF 3. Furthermore, this

ratio has large values in the vicinity of proplyds. To get a quantitative measure of the density, we fitted the H_2 lines corrected for the foreground and internal PDR extinction as well as the H_2 line ratio of 1–0 S(1)/2–1 S(1) observed in the five templates employing the Meudon PDR Code [23]. The Meudon PDR code (Le Petit et al. 2006) can fit the observed line intensities to grids of model PDRs. In this paper, we employ the isochoric model to estimate the gas density. For the isochoric model, which assumes a constant gas density, we first fit all the H_2 line intensities corrected using both the foreground and intermingled formalisms, and then the ratio of 1–0 S(1)/2–1 S(1) obtained with both formalisms, keeping the radiation field and gas density as free parameters. We fix the cloud size expressed as visual extinction A_V to 10 for all the fits. Furthermore, since the H_2 emission in the atomic region and the dissociation fronts belongs to the edge-on PDR, whose brightness at the PDR surface mimics those of an edge-on PDR seen under an inclination ranging from 1–8° (Sect. 6.3.2), we correct the observed fluxes associated with these regions for this geometrical effect. Adopting an inclination angle of 4°, we divide the observed fluxes by a factor of 14 (a geometrical factor in line intensities of $1/\sin(\theta)$ where θ is the inclination angle of the PDR. For $\theta = 4°$, the factor is equal to 14). We highlight that this is a pure geometrical factor that underestimates the real flux. We find that the extinction correction formalism (i.e. foreground or intermingled) does not influence the fit results. The best-fit model, considering all lines, results in a gas density of 3.5×10^4 cm^{-3} in the H II region, $10^3 - 3.5 \times 10^3$ cm^{-3} in the atomic PDR, $10^4 - 3.5 \times 10^4$ cm^{-3} in DF 1 and DF 2, and 10^4 cm^{-3} in DF 3. When considering the line ratio, the best-fit model results in a gas density of $3.5 \times 10^4 - 10^5$ cm^{-3} in the H II region, $10^3 - 3.5 \times 10^3$ cm^{-3} in the atomic PDR, 3.5×10^4 cm^{-3} in DF 1 and DF 2, and 10^4–3.5×10^4 cm^{-3} in DF 3. We remind the reader that the H_2 emission in the H II region originates from the background face-on PDR in OMC-1 (see Fig. 14). Finally, it is worth pointing out that adopting an inclination angle of 8° leads to gas densities from the model fits that are consistently higher by a factor of about 3 compared to an inclination angle of 4°.

We furthermore analyse the H_2 excitation diagrams resulting. Figure 15 presents the excitation diagrams for each template spectrum, where we plot the upper state energy of the transition (E_u/k) versus the normalised column density (N_u/g_u), where N_u is the upper state column density and g_u is the statistical weight of the upper state energy level. We create these excitation diagrams using the H_2 fitting tool in the Photodissociation Region Toolbox (PDRT; Pound & Wolfire 2023)[24]. The tool allows for fitting a one- or two-temperature model and the ortho-to-para ratio (OPR). Here, we analyse the excitation diagrams of $v = 0$ and $v = 1$ vibrational levels for which lines are strong. To get an estimate of the excitation temperature and column density in the five templates, we fitted the excitation diagram of the 0–0 S, 1–0 Q, 1–0 S, 1–0 O, and 1–1 S series independently. We find that using a single temperature and the LTE OPR value of 3 gives the best fit results. We further note that for lines in the $v = 0$ and 1 vibrational series analysed here, the dominant excitation mechanism is radiation – IR radiative cascade of FUV-pumped H_2– rather than collisions. Therefore, the temperatures resulting from these diagrams represent the excitation temperatures rather than the gas temperature. The excitation temperatures and the column densities obtained from fitting the excitation diagrams are presented in Table 4. Lastly, we note that the excitation temperatures obtained from the excitation diagrams in DF 2 and DF 3 are similar to each other but distinct from that in DF 1 implying that the physical properties of DF 2 and DF 3 differ from those of DF 1. A forthcoming paper will analyse the H_2 excitation diagrams based on both the NIRSpec and MIRI IFU PDRs4All observations and thus will include both the collisionally excited levels and FUV pumped levels (Sidhu et al., in prep.).

6.5. CI emission lines

Given the difference between the [C I] 0.985 μm line and the [Fe II] 1.644 μm line delineating the IF and the resemblance between the [C I] 0.985 μm line and the O I 1.317 μm line just beyond the IF, we confirm that the C I originates in the neutral gas beyond the IF. While there is a good resemblance between the [C I] 0.985 μm line and the H_2 emission, enhanced [C I] emission is observed just beyond the IF, similar as for the O I 1.317 μm emission. We find that the ratio of [C I] 0.985/H_2 1–0 S(1) (not corrected for foreground extinction) varies between 0.21 and 2.05 and is <0.9 in the molecular PDR (Fig. 11). This is a much smaller range than observed by Walmsley et al. (2000), who reported ratios between 0.2 and 6, and is likely due to their larger FOV. We also detect C I recombination lines at 1.069 and 1.175 μm (Fig. B.1), which, together with the [C I] 0.983 and 0.985 μm lines, provides an estimate for the electron temperature, T_e, and the gas density, n_H (see Appendix G for details).

First, we can determine whether case A or case B recombination theory applies based on the 1.0696/1.1759[25] line ratio as it is significantly distinct between both cases (Escalante & Victor 1990; Walmsley et al. 2000). However, the observed (extinction corrected) 1.0696/1.1759 line ratios give mixed results (Appendix G). As the observed (extinction corrected) 0.984/1.0969[26] line ratios are consistent with either case A or case B, we estimate the optical depth of a UV resonance line for the high density conditions relevant for the Bar and find it to be optically thick (Appendix G). We thus apply case B recombination theory. The observed extinction corrected 0.984/1.0969 line ratios then results in electron temperatures, T_e, of approximately 2500, 2300, 2900, 6800, and 5600 for, respectively, the H II region, atomic PDR, DF 1, DF 2, and DF 3 templates (Appendix G). Given the uncertainties on the line ratio, the electron temperatures derived for the H II region, the atomic PDR, and DF 1 templates are similar to each other but clearly distinct from those derived for the DF 2 and DF 3 templates (which are also similar to each other within the uncertainties). We note that the emission lines we detect from DF 1 may come from the face-on PDR of the background OMC-1 (Sect. 7). In agreement with the study by Walmsley et al. (2000), the derived electron temperatures are surprisingly high, much higher than temperatures derived from the pure rotational lines of H_2 (~400 K; Allers et al. 2005; Van De Putte et al. 2024) and millimeter-wave carbon recombination lines (mmCRLs; ~500–600 K; Cuadrado et al. 2019).

[23] We note that the Meudon PDR code is part of the interstellar medium database, ISMDB, a web-based fitting tool to fit observations to PDR models. The ISMDB is one of the Science Enabling Products of the PDRS4All ERS programme (Berné et al. 2022), https://pdrs4all.org

[24] The H_2 fitting tool is a Science Enabling Product of the PDRs4All programme, https://pdrs4all.org

[25] The 1.0696 intensity is the sum of the 1.0687 and 1.0696 μm line intensities and the 1.1759 intensity is the sum of the 1.1752 and 1.1758 μm line intensities (Appendix G).

[26] The 0.984 intensity is the sum of the 0.983 and 0.985 μm line intensities (Appendix G).

If all the C I emission results from recombination (see below), these results can be interpret as the carbon NIR recombination lines arising from the hot irradiated surface of small clumps. Unfortunately, as the C I 1.0696 μm line is very weak, we cannot produce a line intensity map of this transition nor a map of the C I electron temperature in order to visually detect clumps. Based on PDR modelling for a typical radiation field, G_0, of 5×10^4 and a wide range of densities (Wolfire et al. 2010, 2022), we conclude that high gas densities ($n \approx 2$–5×10^6 cm^{-3}) are required to reproduce a mean electron temperature, $\langle T_e \rangle = \int T n_e n_{C^+} T^{-0.6} \mathrm{d}z / \int n_e n_{C^+} T^{-0.6} \mathrm{d}z$, of 2000–3000 K, similar to the derived electron temperatures for the H II region, the atomic PDR, and DF 1 templates. However, these model calculations as well as model calculations for a radiation field, G_0, of 1×10^5 and a wide range of densities produce mean electron temperatures, $\langle T_e \rangle$, that are below 4000 K which is significantly lower than those derived for DF 2 and DF 3. The high temperature of the clump reflects the importance of heating by collisional de-excitation of UV pumped H_2 vibrational levels at high densities (Burton et al. 1990). As the dominant cooling transition ([O I] 63 μm) has a critical density of $\sim 3 \times 10^5$ cm^{-3}, cooling cannot keep up with the increased heating and the temperature has to rise to ~5000 K to allow other cooling mechanisms to take over, including through dust radiative cooling and cooling through other (optical) gas lines. Given that the H_2 emission comes from a deeper layer in the PDR with respect to the C I emission, it naturally traces lower temperatures. Moreover, we note that the C I recombination emission is weighted by the carbon emission measure (i.e. proportional to $n^2 L$ with n the gas density and L the depth) and is thus more sensitive to higher density gas whereas the H_2 pure rotational emission is sensitive to the column density, $N = n L$, rather than the density n. The required gas densities to reproduce the C I electron temperature are significantly higher than the gas densities from the NIR H_2 analysis (Sect. 6.4). This suggests then that the H_2 pure rotational lines measure the temperature in the interclump gas and thus do not trace the high density clumps reflecting its sensitivity to the column density, N, rather than the density, n. As the C I emission arises from a very thin layer of a few thousand degree gas, we adopt A_V of 0.5 for this layer (i.e. $N = 1 \times 10^{21}$ cm^{-2}) to derive the gas density, n_H, from the 0.984 μm line intensity (Eq. (G.3)). We obtain densities of 2.1, 5.2, 1.6, 3.5, and 5.3×10^8 cm^{-3} for respectively, the H II region, the atomic PDR, DF 1, DF 2, and DF 3 templates. This is three to four orders of magnitude higher than the gas densities derived from the NIR H_2 analysis (Sect. 6.4). We note that the derived electron temperatures and gas densities for the clumps results in clumps' pressure that much exceeds the pressure of the inter clump medium. Hence, the clumps must be gravitational bound in order to survive or they are transient.

It is clear that the derived C I electron temperatures and densities poses several issues. However, it relies on the assumption that the upper state 2p ^{1}D$_2$ of the 0.982 and 0.985 μm lines is populated solely by radiative recombination and cascade while additional excitation mechanisms would reduce both the derived temperatures and densities. Three other excitation mechanisms are possible. First, ultraviolet absorption and fluorescence via transitions at 1277.245 Å (fluorescence fraction = 0.0106), 1280.135 Å (fluorescence fraction = 0.00695), and 1656.928 Å (fluorescence fraction = 0.000236). Second, direct electron-impact excitation ($e^- + 2p\ ^3P \rightarrow 2p\ ^1D + e^-$; Zatsarinny et al. 2005; Zatsarinny & Bartschat 2013). Third, photodissociation of CO, which occurs via predissociation of far-UV lines (van Dishoeck & Black 1988; Visser et al. 2009; Guan et al. 2021). Combined with recombination, these three excitation mechanisms ensure that the near-IR [C I] lines can be excited not only in the nebula and the ionised carbon zone of the atomic PDR, but also through the neutral carbon layer, and on into the molecular PDR where CO is photodissociated. The relative contribution of these excitation mechanisms and their influence on the C I analysis as described above will be explored in a future paper.

6.6. AIB emission

The components of the 3–4 μm AIB emission in the Bar exhibit variations in intensity, which we discuss in Sect. 6.6.1, and variations in profiles, which we discuss in Sect. 6.6.2. The comparison of the 3–4 μm AIB emission to the mid-IR AIB bands is reported in Chown et al. (2024).

6.6.1. AIB intensity variations

We have performed two spectral decompositions of the AIB emission, which are applied to every pixel of the NIRSpec mosaic. First, we employ an updated version of PAHFIT (Smith et al. 2007; Lai et al. 2020)[27]. In PAHFIT-based models, the AIBs are represented by Drude profiles. Second, we have employed a Gaussian decomposition of the AIB emission in the 3.2–3.7 μm region. The resulting fit for both methods reproduces the observations very well (Fig. 16). In contrast to the PAHFIT method, which uses 7 Drude profiles, the Gaussian decomposition also includes one Gaussian representing the underlying plateau emission and one Gaussian representing the extended red wing of the 3.29 μm AIB. The remaining components are remarkably similar for both decomposition methods. Details on both spectral decompositions are given in Appendix H.1. While neither decomposition method provides a physical decomposition, it allows for a systematic analysis of the AIB emission characteristics. The intensity maps of the AIB components are shown in Fig. 17 and their emission along the cut in Fig. 18.

Most AIBs (all but the 3.40 and 3.42 μm AIBs) mimic the global morphology as seen by the total AIB emission (Fig. 7): a sharp rise at the PDR front, a (broad) plateau in the atomic PDR with a width of about 6.5″ (~1.3×10^{-2} pc), after which a steady decline sets in. This decline levels off towards the south end of the mosaic/cut, reaching brightness levels as observed in the H II region, where the AIB emission originates from the background face-on PDR OMC-1. The latter is in contrast with the 3 μm continuum emission which is much higher in the H II region than in the molecular PDR (see Sect. 5.1). The exceptions to the global AIB morphology are the 3.40 μm AIB and the 3.42 μm AIB (to a slightly lesser extent), which peak in DF 3, instead of the atomic PDR, and show enhanced emission in DF 2 but not in DF 1 compared to the 3.3 μm AIB. The 3.4/3.29 integrated intensity ratio[28] is 0.09–0.11 in the H II region, the atomic PDR and DF 1 templates, whereas values of 0.15 and 0.18 are observed in the DF 2 and DF 3 templates, respectively (for the Gaussian decomposition, Table 1). In addition, while the 3.46 and 3.51 μm AIBs peak in the atomic PDR, these AIBs also show enhanced emission in DF 2 and DF 3, relative to that in the atomic PDR, with respect to the 3.29 μm AIB. Hence, the 3.40, 3.42, 3.56, 3.46, and 3.51 μm AIBs show a less steep increase at the PDR front than the 3.29 μm AIB (of about 4 compared to an increase of about 5 seen in the 3.29 μm AIB emission).

[27] Available at https://github.com/PAHFIT
[28] Calculated by the ratio of the (3.39+3.40+3.42)/(3.29) AIBs.

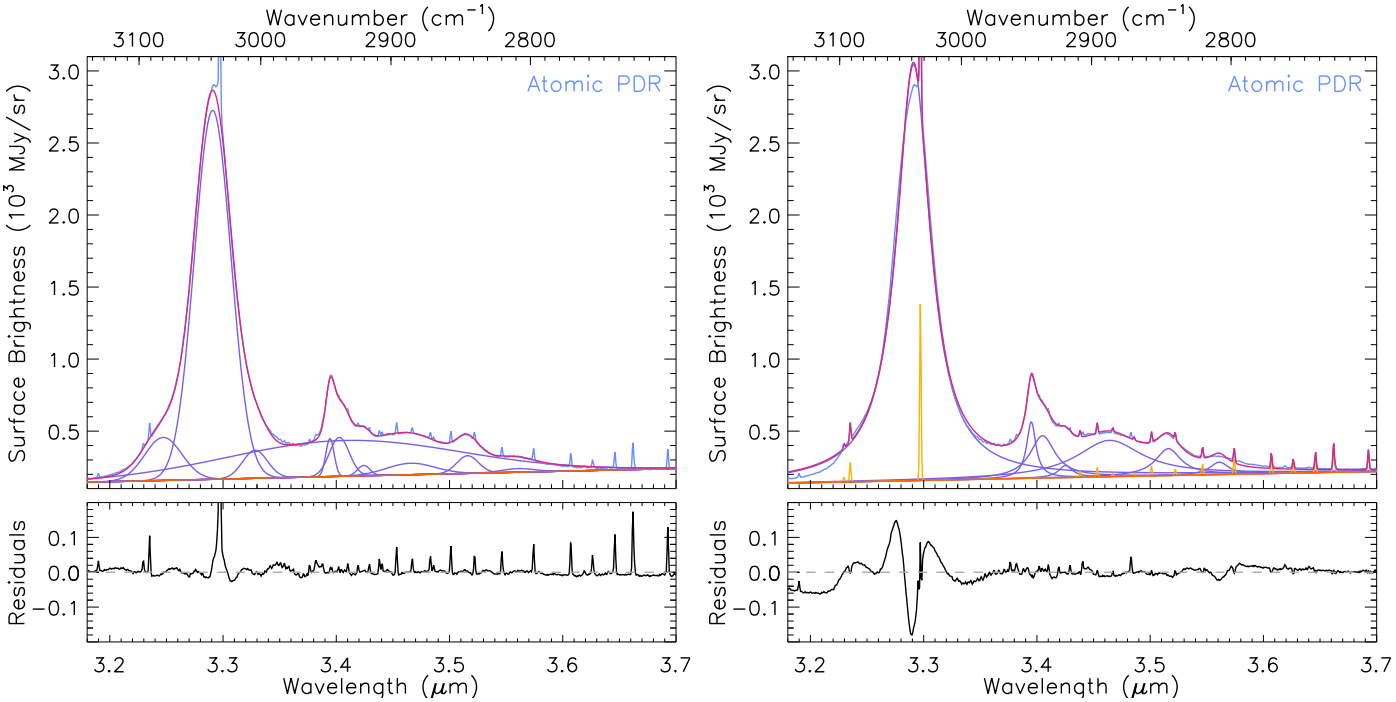


Fig. 16. Spectral decomposition of the AIB emission for the atomic PDR by a Gaussian decomposition (left) and by PAHFIT (right). The dust continuum emission is represented by the orange line, the AIB components by the purple profiles, and emission lines by the yellow Gaussians (for the PAHFIT decomposition; the Gaussian decomposition method removes the lines prior to fitting).

The plateau emission (in the Gaussian decomposition) has a spatial distribution similar to the 3.29 μm AIB, but shows slightly enhanced emission in DF 2 and DF 3 (albeit significantly less than the enhanced emission seen in the 3.40 and 3.42 μm AIBs). Hence, based on its spatial distribution we cannot conclude whether or not the plateau is independent of the superposed features as is observed for the plateaus between 5–10, 10–15, and 15–20 μm (Bregman et al. 1989; Peeters et al. 2012, 2017; Stock & Peeters 2017). Proplyd 203–506 stands out in the AIB maps. Namely, it shows enhanced emission in the 3.40 and 3.42 μm AIBs with respect to the other AIBs, and a 3.3 μm AIB intensity comparable to the lowest seen 3.3 μm AIB intensity in the atomic PDR.

Lastly, we tentatively detect the aromatic CD vibrational mode at 4.35 μm in the atomic PDR and DF 1, and the aliphatic CD vibrational mode at 4.644 μm in potentially all templates (see Sect. 4.1 and Appendix H.2 for details). The aliphatic CD vibrational mode is strongest in the atomic PDR, followed by DF 1, the H II region, DF 2, and is weakest in DF 3 (Table H.2; see Appendix H.2 for details). As the band at 4.35 μm is not well defined (see Sect. 4.1), we refrain from estimating its intensity though we note that it is most easily discerned in the atomic PDR and DF 1 that also exhibit the strongest 4.644 μm band. The ratio of the 4.644 μm band to the total AIB emission in the 3.2–3.7 μm range is 8.2, 6.3, 6.1, 2.8, and 2.4 $\times 10^{-3}$ for the H II region, the atomic PDR, DF 1, DF 2, and DF 3 templates (Table 1) and thus is significantly lower in DF 2 and DF 3 compared to the other templates. A similar pattern is seen in the 4.644/3.29 AIB ratio whereas the 4.644/3.40 AIB ratio is highest in the atomic PDR, closely followed by the H II region, subsequently DF 1 and significantly lower in DF 2 and DF 3 (Table 1). We further note that the excess broadband emission is strongest in the atomic PDR and decreases deeper in the PDR while it is (nearly) absent in the H II region.

6.6.2. Profile variations

Not only do the relative AIB intensities change across the mosaic, so do the AIB band profiles (Fig. 19). The 3.29 μm AIB has a variable width with the full-width-half-maximum (FWHM) ranging from 37.4 cm^{-1} in the atomic PDR to 42.4 cm^{-1} in DF 3 (see Table 1 for FWHM values for all templates). DF 1 shows a band profile similar to that observed in the H II region and the atomic PDR. The extra broadening in DF 2 and DF 3 relative to the other three templates is largely carried by the blue wing. As a consequence, the peak position seems to shift to slightly bluer wavelengths in the DF 2 and DF 3 templates albeit quantifying this shift is hampered by the atomic emission lines (Pfδ, He I recombination lines) superposed on the peak of the AIB. Despite the observed profile variations, all templates exhibit a class A band profile in the classification scheme proposed by van Diedenhoven et al. (2004), and thus showcase profile variability within class A. We note that also the mid-IR AIB band profiles exhibit variations (Chown et al. 2024). Similarly, despite the profile variations, the mid-IR AIBs exhibit a class A band profile except for the 11.2 μm AIB which displays a class A profile in the H II region, the atomic PDR, and DF 1 and a class B profile in DF 2 and DF 3 (Chown et al. 2024).

Profile variations are also detected for the 3.4 μm AIB. This band shows an asymmetric profile with a red wing and consists of three components (at 3.39, 3.40, 3.42 μm, see Table H.1). Comparison of the 3.4 μm AIB profile in the template spectra indicate enhanced emission in the red wing of the 3.40 μm component and thus enhanced broadening of the band in DF 2 and DF 3. Similar to the 3.29 μm AIB profile, DF 1 displays a similar profile to that observed in the H II region and the atomic PDR. Given that numerous H I recombination lines (from the Humphreys series) and H_2 lines are superposed on this AIB,

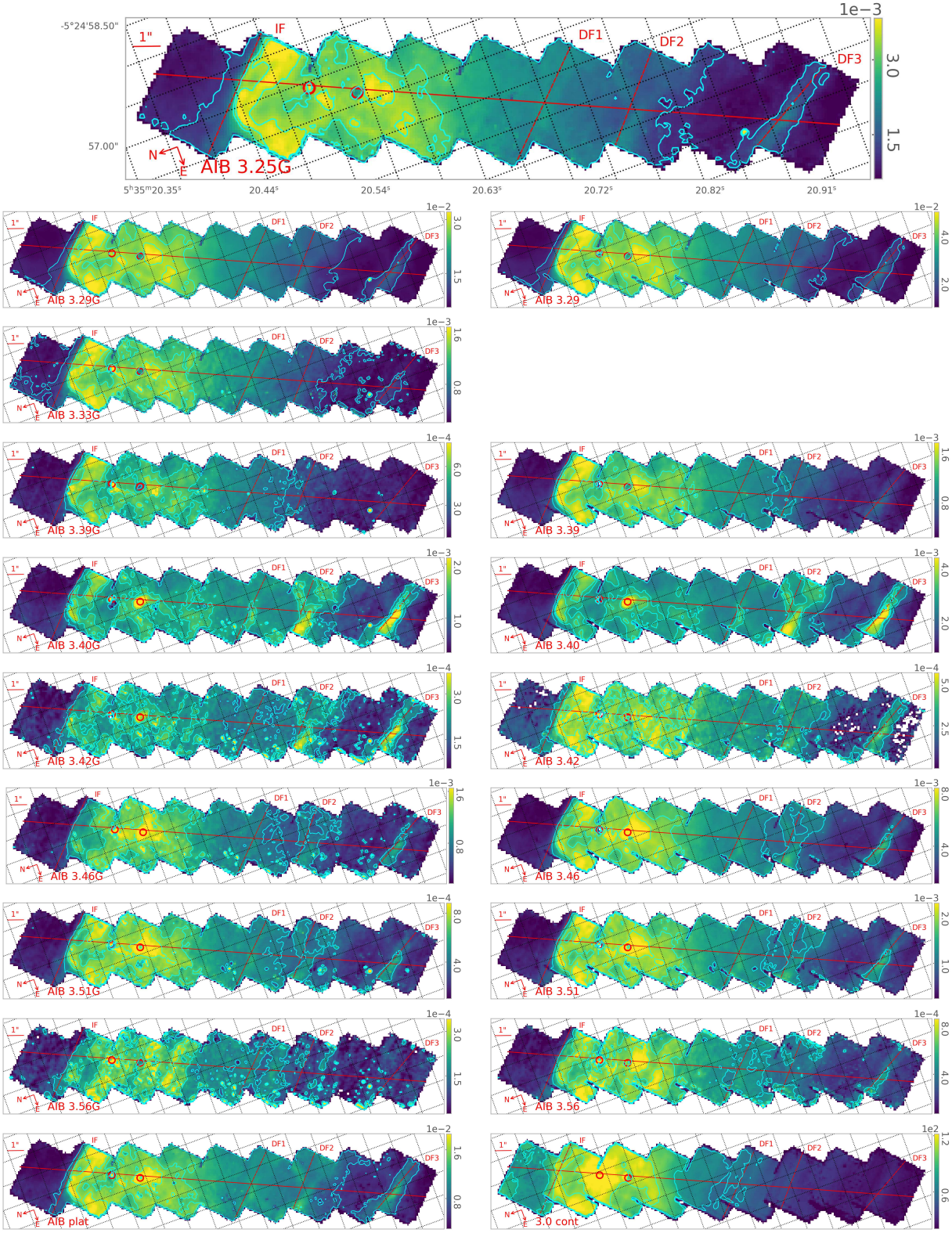


Fig. 17. Spatial distribution of the AIB components in the 3.2–3.7 μm range from the Gaussian decomposition (top and left panels) and PAHFIT decomposition (right panels). 'AIB plat' refers to the plateau emission (bottom panel, left) and '3.0 cont' to the continuum emission at 3.0 μm (bottom panel, right). Units are erg cm^{-2} s^{-1} sr^{-1}, except for the 3.0 μm continuum map, which is in units of MJy sr^{-1}. We set the colour range from the bottom 0.5% to the top 99.5% of data for each map, excluding values of zero, edge pixels, and the two proplyds (as well as the surrounding region of the proplyds for the continuum). White pixels inside the mosaic indicate values of zero reflecting either the component was not used in the fit or issues with the data. The nearly horizontal red line indicates the NIRSpec cut and the nearly vertical red lines indicate from left to right the IF and the DFs (DF 1, DF 2, DF 3). The two proplyds are indicated by the circles. Contours show the 30, 78, 94% of the data for the 3.25G, 3.29/3.29G, and 3.33G components as well as the AIB plat, 50, 78, 93% for the 3.39/3.39G and 3.56/3.56G components, 35, 78, 93% for the 3.40/3.40G and 3.42/3.42G components, 45, 78, 94% for the 3.46/3.46G and 3.51/3.51G components, and 50, 68, 85% for the continuum emission at 3.0 μm. The continuum emission at 3.0 μm from the Gaussian decomposition is shown in Fig. 7.

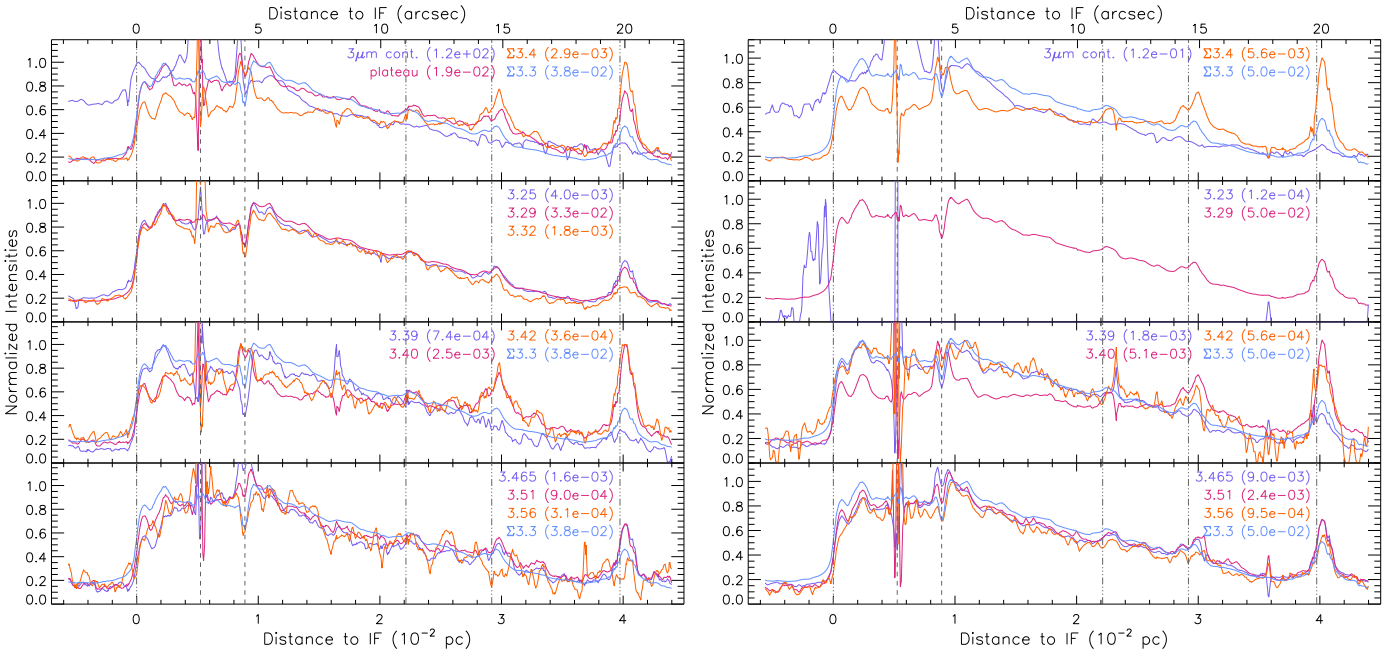


Fig. 18. Normalised AIB and continuum intensities from the Gaussian decomposition (left) and the PAHFIT decomposition (right) as a function of distance to the IF (0.228 pc or 113.4″ from θ^1 Ori C) along a cut crossing the NIRSpec mosaic (see Fig. 1). Normalisation factors are listed between brackets for each intensity. As the cut is not perpendicular to the IF and distances are given along the cut, a correction factor of cos(19.58°)=0.942 needs to be applied to obtain a perpendicular distance from the IF. Σ3.3 reflects the brightness of the 3.25, 3.29, 3.33 μm or 3.23 and 3.29 μm AIBs combined for, respectively, the Gaussian and PAHFIT decomposition. Σ3.4 reflects the brightness of the 3.40, and 3.42 μm AIBs combined. No extinction correction is applied. The dash-dot-dot-dot vertical lines indicate the position of the IF, DF 1, DF 2, and DF 3, respectively, from left to right. The dashed vertical lines indicated the location of the proplyds 203–504 (left) and 203–506 (right). Units are erg cm^{-2} s^{-1} sr^{-1} except for the 3 μm continuum which is in units of MJy sr^{-1}.

a detailed analysis of the 3.4 μm AIB will be performed in a forthcoming paper (Dartois et al., in prep.).

6.6.3. Comparison to previous observations

The spectral inventory of the AIB emission in the 3.2–3.7 μm range is consistent with prior high quality observations of the Orion Bar (Sloan et al. 1997). Likewise, the observed 3.4/3.29 intensity ratios (Table 1) are consistent with earlier reports for the Orion Bar by Geballe et al. (1989) and Sloan et al. (1997). The latter authors also reported a widening (towards the red) of the 3.4 μm AIB into the molecular PDR. To first order, this is consistent with our results but the strength of their 'excess' emission (with respect to the 3.4 μm AIB in the H II region) peaks near 10″ from the IF after which it steadily declines whereas we detect the broadest profile in DF 3 at a distance of 19.8″. In addition, as our observations have unparalleled angular resolution, the radial profiles of the AIB intensities with distance from θ^1 Ori C (Fig. 18) exhibit significant more detail compared to prior observations (Geballe et al. 1989; Sloan et al. 1997).

To our knowledge, the 3.1–4.9 μm broad emission or the 3.8 μm band has not been observed before (Sect. 4.1). In contrast, the bands near 4.4 and 4.6 μm have been detected in the Orion Bar and were attributed to deuterated PAHs (Peeters et al. 2004; Onaka et al. 2014). Following Peeters et al. (2004, i.e. assuming that the integrated absorbance values of the corresponding C-H/C-D modes are similar), we obtain an aliphatic D/H ratio (as probed by 4.64/3.40 bands) of 20.5, 22.5, 15.8, 5.4, and 4.1×10^{-2} in the H II region, the atomic PDR, DF 1, DF 2, and DF 3 templates. This is in contrast to the reported D/H ratio of ∼ 1 reported by these authors. Instead, this derived aliphatic D/H ratio is more in line with the combined aliphatic and aromatic D/H ratio of 0.17 reported by these authors[29]. A quantitative comparison with the results of Onaka et al. (2014) is not possible as these authors applied a different decomposition method[30]. However, these authors reported D/H ratios an order of magnitude lower than those of Peeters et al. (2004). Specifically, they reported an aliphatic D/H ratio (as probed by 4.64/(3.42+3.48) bands) of 0.04 which is of the same order of magnitude as our 4.64/(3.39+3.40+3.42+3.46) ratios using the PAHFIT decomposition (ranging from 0.03 to 0.007, though remember different decomposition methods are used).

6.6.4. Photochemical evolution

The 3 μm region is characteristic for the aromatic and aliphatic C-H stretching mode (e.g. Allamandola et al. 1989). The aromatic CH stretching modes are very susceptible to resonances with combination bands (Maltseva et al. 2015, 2016; Mackie et al. 2015, 2016) and this interaction dominates their profiles (Mackie et al. 2022). Smaller PAHs have more asymmetric profiles, that is, a less steep blue wing and enhanced red wing, reflecting their higher internal energies upon photon absorption (Tielens 2021; Mackie et al. 2022). The observed widening of the asymmetric 3.4 μm band in DF 2 and DF 3 thus may arise

[29] The combined aliphatic and aromatic ratio was probed by the (4.4+4.6)/(3.3+3.4+3.5) using the Gaussian decomposition. Using the nomenclature of this paper, this denominator reflects the sum of all Gaussian components in the 3.2–3.7 μm range except the plateau emission.

[30] These authors used Lorentzian profiles for the 3.29, 3.41, and 3.48 μm bands and did not assume a plateau component.

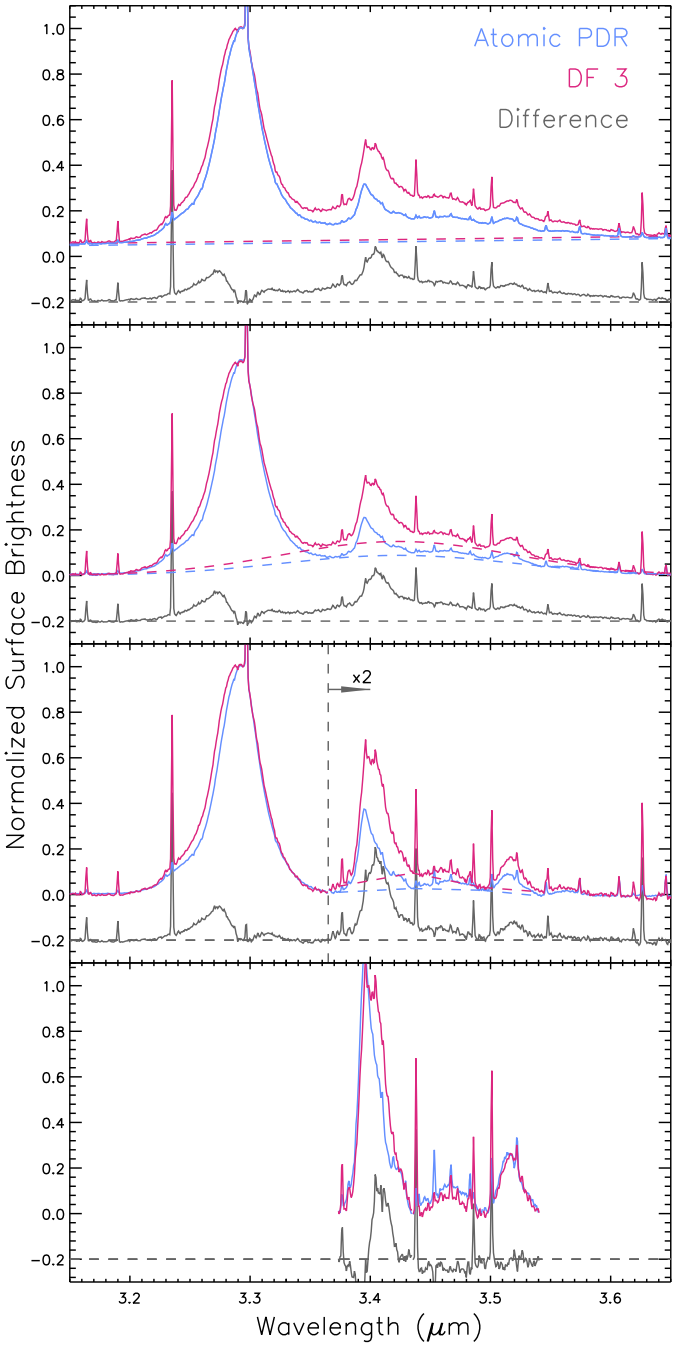


Fig. 19. Comparison of the AIBs in the atomic PDR (blue) and DF 3 (red). The difference in their normalised emission is given in grey and the grey dashed line indicates the zero level for the difference spectrum. Top to bottom: template spectra (solid lines) and their respective linear dust continuum (coloured dashed lines); continuum-subtracted template spectra (solid lines) and their respective plateau emission (coloured dashed lines); (continuum+plateau)-subtracted template spectra (solid lines) and their respective local continua for the weaker AIBs (coloured dashed lines); (continuum+plateau+local continuum)-subtracted template spectra. The template spectra are normalised on the peak intensity of the 3.29 μm AIB in the top three panels, and of the 3.40 μm AIB in the bottom panel.

from an enhanced population of smaller PAHs. The corresponding broadening of the roughly symmetric 3.29 μm band (largely driven by the blue wing) may then arise from the same enhanced population of smaller PAHs. Regions with broader AIB profiles (with respect to the atomic PDR) also show enhanced 3.4/3.29 intensity ratios which traces the aliphatic-to-aromatic ratio (or the degree of aromaticity). The aliphatic-to-aromatic ratio, as traced by the 3.4/3.29 intensity ratio, is known to decrease with increasing intensity of the FUV radiation field (Geballe et al. 1989; Joblin et al. 1996; Sloan et al. 1997; Mori et al. 2014; Pilleri et al. 2015) reflecting that aliphatic bonds are less stable than aromatic ones. Combined with the fact that smaller PAHs are less stable than larger ones, the observations point towards a more fragile population of complex hydrocarbons in DF 2 and DF 3 compared to the complex hydrocarbon population in the H II region (i.e. the background PDR), the atomic PDR, and DF 1. This suggests a UV-driven photochemical evolution of the complex hydrocarbon population that eliminates the more fragile hydrocarbon species near the surface of the PDR which is subjected to a more intense FUV radiation field.

In contrast, the tentative detection of high aliphatic D/H ratios near the surface of the PDR and low ratios deep in the molecular PDR argue against a slow loss of deuterated PAHs as material reaches the surface of the PDR; that is, the presence of PADs in the surface layer of the PDR is not inherited from its past (i.e. from the molecular cloud). Instead, the PAH D enhancement is a local effect that seems to be driven by UV radiation and/or density (as it is strongest in the atomic PDR template). In addition, we note that the aliphatic CD stretch is significantly stronger than the aromatic CD stretch, consistent with prior observations (Peeters et al. 2004; Onaka et al. 2014; Doney et al. 2016) suggesting that the D enhancement is more favourable on aliphatic than aromatic sites. The expected difference in binding energy between hydrogen and deuterium is ~440 cm^{-1} (Allamandola et al. 1989; Wiersma et al. 2020) and, thus, too small to explain the observations. In addition, this energy difference leads to enhanced H scrambling and H loss compared to D while the molecule is exposed to a stronger UV field (Wiersma et al. 2020). Moreover, these authors found that D scrambling favours the migration to a strongly bound aromatic site (instead of an aliphatic site) which could lead to increased aromatic deuteration with respect to aliphatic deuteration. This is in contrast with the observations presented here. It should be noted that the interpretation or possible mechanism to increase aliphatic CD is still speculative and further investigations are warranted. Hence, the PAH D enhancement will be further explored in a forthcoming paper.

7. Discussion

The Bar has served as the template PDR to develop the first PDR models (Tielens & Hollenbach 1985a,b). These theoretical studies predicted a global stratification as a function of depth in the PDR. Tielens et al. (1993) provided the first observational evidence of this stratification and reported an offset between the 3 μm AIB emission, the H_2 1–0 S(1) emission, and the J = 1–0 CO emission. The PDRs4All NIRSpec observations provide a more diverse and detailed picture of the Bar anatomy on spatial scales of 0.075″ – 0.173″. The global stratification (and geometry) as seen with NIRSpec is summarised below, illustrated in Fig. 14, and quantified in Table 2. We note that all distances are quoted along the NIRSpec cut (see Sect. 5.1).

– Closest to θ^1 Ori C, we observe the He-IF at an approximate projected distance of 0.222 pc. The He-IF is resolved and displaced from the H-IF by about 0.4–0.5 × 10^{-2} pc (1.8″–2.5″) in the Huygens region. The NIRSpec mosaic does not cover the peak emission from the He I recombination lines.

– The H-IF is traced by the peak emission of the H I recombination lines (at 113.276″ or d_{proj} = 0.2274 pc from θ^1 Ori C). The sharp decrease towards θ^1 Ori C within the NIRSpec mosaic is likely caused by the gas being accelerated away once it is ionised. The H I recombination line emission decreases away from θ^1 Ori C but does not go to zero due to the foreground H II region (i.e. the H II region in front of the atomic and molecular PDR along the line of sight). As for the He I emission, the NIRSpec mosaic does not cover the peak H I emission within the H II region which, is located about 24″ in front of the H-IF (e.g. Pellegrini et al. 2009).
– The IF is well traced by the [O I] 6300 Å and [Fe II] 1.644 μm emission. We note that this is displaced from the H-IF by 0.1″ or 0.02 × 10^{-2} pc. Enhanced emission of [O I] 6300 Å is also observed in the atomic PDR, which is mostly confined to the region surrounding the proplyds and the filaments. While part of this emission is associated with the proplyds and their jets, the strongest emission is seen in the N-SE filament, which is, to our knowledge, not associated with the proplyds and is parallel to the secondary ridge in the IF. In contrast, the [Fe II] 1.644 μm only shows enhanced emission in the direction of the jet associated with proplyd 203–506. We further note that the N-SE filament is very strong in the O I 1.317 μm emission, but given the lack of enhanced emission in the [Fe II] 1.644 μm line, undulation effects in the surface of the Bar as the prime reason of the observed enhancement in the O I emission can be excluded. Instead, we attribute the enhanced emission to local acceleration zones (Sect. 6.3.1).
– The AIB emission is an excellent tracer of the atomic PDR. The strength of the AIB emission is set by the strength of the FUV radiation field required for the excitation process and the column density of the carriers. The steep increase in its emission (up to 65%) over a very small distance (∼1″) centred at the IF thus indicates the (very sharp) onset of the atomic PDR. Along the NIRSpec cut, the AIB emission remains flat for about 6.5″ or ∼1.3 × 10^{-2} pc, after which it slowly decreases. As the strength of the FUV radiation decreases with depth into the PDR due to dust opacity, the lack of a decrease in AIB emission beyond the onset of the atomic PDR, as well as the small-scale structure observed in the AIB emission, reveals a complexity of the atomic PDR in terms of geometry and small-scale structure that is not captured by 1D PDR models. The AIB emission (primary ridge) peaks at 113.7″ in contrast with earlier studies that reported the AIB emission peaking at 118 and 117″ from θ^1 Ori C (Salgado et al. 2016; Knight et al. 2022). This is attributed to their use of lower angular resolution observations, as well as probing a different location on the Bar. Habart et al. (2024) derived an atomic gas density of 5–10 × 10^4 cm^{-3}. The (maximum) strength of the FUV radiation field impinging on the PDR front can be traced by the fluorescent lines (O I 1.129, 1.317 μm and N I 1.2292 μm) and varies across the PDR front between G_0 = 2.2 to 7.1 × 10^4.
– The transition from the atomic to the molecular PDR is highly structured and displays three dissociation fronts that are parallel to the IF (see also Habart et al. 2024). The rise in the H_2 emission is very sharp (with factors of ∼3, 6, and 10 over a very small distance (0.5″)). These ridges (at a distance of (2.21, 2.92, 3.97) × 10^{-2} pc or 11.03″, 14.55″, 19.80″) represent edge-on portions of the DF, with DF 2 nearly coinciding with the average H_2 emission in the Bar (Habart et al. 2024). Enhanced AIB emission is seen at the three DFs which is lightly displaced from the DFs by (0.02, 0.06, 0.04) × 10^{-2} pc (0.1″, 0.3″, 0.2″), in the direction away from the atomic PDR.

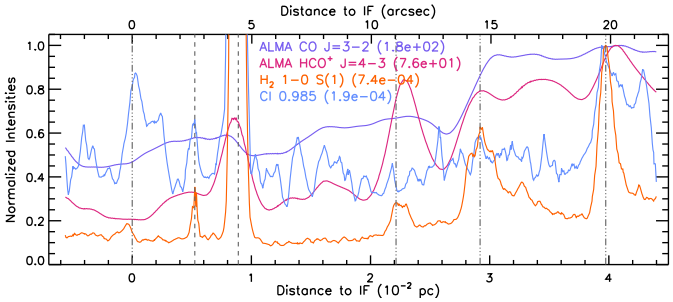


Fig. 20. Comparison of the NIRSpec H_2 1–0 S(1) and C I 0.985 μm observations (in erg cm^{-2} s^{-1} sr^{-1}) with the ALMA observation at 1″ resolution of the HCO^+ J=4–3 line integrated intensity (in K km s^{-1}) and the CO J=3–2 line peak temperatures (T_{peak}, Goicoechea et al. 2016). Shown are normalised line intensities as a function of distance to the IF (0.228 pc or 113.4″ from θ^1 Ori C) along a cut crossing the NIRSpec mosaic (see Fig. 1). As the cut is not perpendicular to the IF and distances are given along the cut, a correction factor of cos(19.58°)=0.942 needs to be applied to obtain a perpendicular distance from the IF. Normalisation factors are listed between brackets for each intensity. No extinction correction is applied. The dash-dot-dot-dot vertical lines indicate the position of the IF, DF 1, DF 2, and DF 3, respectively, from left to right. The dashed vertical lines indicated the location of the proplyds 203–504 (left) and 203–506 (right).

On top of this large-scale morphology/stratification, we observe numerous smaller-scale structures. The typical size of these structures seem to be largest in the ionised gas tracers (a few arcsecs), whereas in the IF, the atomic and molecular PDR structures of sizes of a few 0.1″ are observed. The IF and PDR front is thus highly irregular, non-uniform, and complex. This is also clearly demonstrated in the PDRs4All JWST images (Habart et al. 2024), as well as optical images (e.g. Weilbacher et al. 2015; Henney 2021). As a consequence, all physical parameters, for example, derived in this paper are very precise, but, at the same time, inaccurate due to their dependence on the exact position (on 0.1″ scale) of the intensity of the tracer used to obtain the physical parameter and the incredible small-scale variation observed in these tracers (as well as the assumptions used for the derivation). In addition, assuming the C I emission arises solely from radiative recombination and cascade, the analysis of the C I emission in the template spectra indicates the presence of very high density clumps embedded in a lower-density gas. Based on HCO^+ J=4–3 observations with an angular resolution of ∼1″, Goicoechea et al. (2016) also reported that the gas density near the DF is very inhomogeneous and clumpy with small-scale structure surrounding, and parallel with, the dissociation front (the DF set by these authors corresponds to DF 2). Along the NIRSpec cut, this HCO^+ emission is strongest at DF 3 and displays slightly weaker emission near DF 1 and DF 2, whereas it is considerably weaker towards the H II region and the atomic PDR (Fig. 20).

We further note that DF 1 behaves uniquely compared to DF 2 and DF 3. We summarise:

1. The extinction from the atomic PDR, $A_{V,bar}$, is about 2–4 times higher towards DF 1 than towards DF 2 and DF 3 (Sect. 6.4).
2. While DF 1 is still visible in the AIB emission map, it is indiscernible in the NIRCam F210M filter (Sect. 5.1,

Habart et al. 2024) nor does it exhibit signs of enhanced dust scattered light (Sect. 4.1).
3. DF 2 and DF 3 display a slightly richer molecular inventory, for example, HD v = 1–0 (Sect. 4.1) and the presence of 6.850 and 6.943 μm AIBs (Chown et al. 2024).
4. The characteristics of the AIB emission towards DF 1 are similar to those for the H II region and the atomic PDR, but quite different from those observed in DF 2 and DF 3. Specifically,
   (a) the FWHM of the 3.3 AIB is similar in the H II region, the atomic PDR, and DF 1 (about 38 cm^{-1}), but significantly lower than that of DF 2 and DF 3 (41–43 cm^{-1}, Sect. 6.6). Similar broadening is observed in DF 2 and DF 3 for MIR AIBs (5.25, 6.2, 7.7, 11.2, and 12.7 μm; Chown et al. 2024).
   (b) the aliphatic-to-aromatic ratio, as probed by the 3.4/3.29 AIB, at DF 1 is similar to that of the H II region and the atomic PDR, but 1.5–1.75 times lower than in DF 2 and DF 3 (Sect. 6.6).
   (c) the 11.2 μm AIB displays a class A profile in the H II region, the atomic PDR, and DF 1 and a class B profile in DF 2 and DF 3 (Chown et al. 2024).
   (d) the aliphatic D/H ratio in DF 1 is similar to that in the atomic PDR and about twice that observed in DF 2 and DF 3 (Sect. 6.6).
5. Within the assumptions, the C I emission indicates the presence of clumps. The electron temperature probed in DF 1 is similar to that in the H II region and the atomic PDR whereas it is significantly lower compared to the electron temperature probed in DF 2 and DF 3.
6. The CO J=3–2 emission intensity is considerably lower in DF 1 than in DF 2 and DF 3 (and similar to the atomic PDR and H II region; Fig. 20; Goicoechea et al. 2016).
7. The HCO^+ J=4–3 and CO J=3–2 emission velocities at DF 1 have two components, one of which is more consistent with emission from the background molecular cloud, OMC-1, than from the Bar (Goicoechea et al. 2016).

Following Goicoechea et al. (2016), we attribute the small-scale variations to pre-existing, turbulently driven density variations in OMC-1 that were amplified by the passage of the shock driven into this core by the stellar feedback of θ^1 Ori C, perhaps guided by the magnetic field structure that will be enhanced parallel to the shock front. Such small-scale structures can be developed during the passage of the shock due to different types of instabilities (Krasnobaev et al. 2016; Krasnobaev & Tagirova 2017; Riashchikov et al. 2022). It is tempting to speculate that the high density clumps are sites for future star formation, however Goicoechea et al. (2016) concluded that their current mass is not sufficient to make them gravitationally unstable.

Furthermore, based on #1, #2, and #7, Habart et al. (2024) concluded that the DF displays a terraced-field-like structure where the three DFs are portion of the DF observed edge-on and with DF 1 located at a larger distance (from us) compared to DF 2 and DF 3 (see Fig. 14). In addition, based on #6 and #7, Goicoechea et al. (2016) suggested that the CO plumes present between the IF and their DF (i.e. DF 2) could be CO gas flows that are photo-ablated from the molecular PDR into the atomic PDR. The location of DF 1 between the IF and the steep increase seen in the CO J=3–2 emission intensity (#6) thus indicates that the depth in the molecular cloud at DF 1 is smaller than at DF 2 and DF 3 and does not reach the C^+/C/CO transition. At the same time, the HCO^+ observations indicate that DF 1 (as well as DF 2 and DF 3) is part of the compressed layers (#5, Goicoechea et al. 2016). The distinct AIB properties in DF 1 (similar to those in the H II region and the atomic PDR templates) with respect to those observed in DF 2 and DF 3 then suggests that i) they are characteristic for depths in the PDR shortwards of the C^+/C/CO transition, or ii) they are due to an increased (and perhaps dominant) contribution of the atomic PDR to the line of sight emission towards DF 1, or iii) both.

Finally, we note that the Bar is primarily illuminated by θ^1 Ori C. Beyond the Bar, O'Dell et al. (2017) reported that the primary illuminating source is θ^2 Ori A instead. The PDRs4All NIRCam images (Habart et al. 2024, their Fig. 3) suggest that the influence from θ^2 Ori A is limited to its nearby environment in the direction of the Bar because of the high density in that direction (see the enhanced emission in a 'box' surrounding θ^2 Ori A in the F335M (red) and F470N (green) filters). In addition, from a qualitative perspective, our observations do not show any indication of additional or primarily ionisation due to the radiation field of θ^2 Ori A. In fact, the decrease of O I 1.317 μm beyond DF 1 is consistent with a geometrical dilution model centred on θ^1 Ori C (Sect 6.3.1). A similar NIRSpec study of the immediate surrounding of θ^2 Ori A would further clarify the response of the gas to the θ^2 Ori A radiation field. We derived several geometrical distances relevant to obtain a comprehensive 3D picture of the Bar based on the O I 1.317 μm emission (Sect. 6.3.2). As discussed above, these are specific for the NIRSpec mosaic and may change slightly for other positions on the Bar.

8. Conclusions

We present JWST NIRSpec IFU spectral imaging data of the proto-typical PDR in the Orion Nebula, the Bar. Our observations probe the 0.97–5.27 μm at a spectral resolution R of ~2700 and approximately cover 3″ by 25″ at an angular resolution of 0.075″–0.173″. At the distance of the Bar, this is equivalent to 1.5–3.46 × 10^{-4} pc. As such, this unprecedented data set showcases both the large-scale and small-scale structure of the interstellar medium subjected to strong FUV radiation of nearby massive stars. In addition, our mosaic encompasses two proplyds, 203–504 and 203–506, and their associated jets and Herbig-Haro object.

These observations reveal a spectacular richness of spectral lines (~600) and aromatic IR bands on top of weak continuum emission. We detect a forest of atomic and ionic lines as well as numerous H_2 ro-vibrational lines. We furthermore report the detection of:

- H_2 pure rotational lines in the vibrational states v = 0, 1, and 2
- ro-vibrational lines of HD v = 1–0
- ro-vibrational lines of CO v = 1–0, v = 2–1
- ro-vibrational lines of CH^+ v = 1–0
- vibrational emission of deuterated aromatic hydrocarbons

Most of these molecular lines are detected for the first time towards a PDR. We provide a line list to facilitate identification of observed lines in future JWST observations. We illustrate the immense diagnostic power provided by the combination of this treasure trove of emission lines and the unprecedented angular resolution through the analysis of the spatial distribution of selected line/band intensities and determine the variations in the physical conditions of the PDR gas and the evolution of complex hydrocarbons.

The observations furthermore reveal the anatomy of the Bar: a large-scale morphology or stratification with distance from θ^1 Ori C and numerous smaller-scale structure, some of which were inaccessible with earlier IR observations. The typical size

of these structures is largest in the ionised gas tracers and smallest for the molecular gas tracers. We highlight in particular:

- the spatially resolved He-IF and the H-IF in the Huygens region for the first time.
- the presence of three dissociation fronts (DFs) which show different characteristics. The increasing internal PDR extinction suggests each of the DFs is located increasingly further from us. Habart et al. (2024) posited that the DF surface is a terrace-field-like structure seen from above in which the 3 DFs are seen as edge-on portions of the DF surface.
- the presence of hot ($T \geq 2000$ K) irradiated surfaces of dense clumps as indicated by the C I emission assuming it solely arises from radiative recombination and cascade.
- the constant density in the atomic PDR.
- the varying aromatic-to-aliphatic ratio and width of the AIBs showcasing the photochemical evolution of the AIB carriers, which is driven by the FUV radiation field.
- the presence of deuterated aromatic hydrocarbons with considerably stronger intensity in the surface layer of the PDR compared to the molecular PDR indicating the D-enhancement is not inherited but rather a local effect.
- enhanced filamentary O I 1.317 μm emission in the jets associated with the two proplyds and in the atomic PDR, which may reflect a local gas acceleration zone.

Our results showcase the complexity of PDRs, and provide very strong constraints on the evolution of the physico-chemical conditions at the critical $H^+/H^0/H_2$ transition and the external boundary conditions of dense molecular condensations. As such, the PDRs4All data set serves as the benchmark to extend PDR models in to the JWST era. The analysis of this data set and the numerous tools developed by the PDRs4All team[31] will assist observers in the analysis of future observations of (unresolved) PDRs, in particular extragalactic objects, while at the same time highlighting the issues encountered when only limited spatial resolution is available.

Acknowledgements. We thank the referee Will Henney for valuable feedback on the manuscript. This work is based on observations made with the NASA/ESA/CSA *James Webb* Space Telescope. The data were obtained from the Mikulski Archive for Space Telescopes at the Space Telescope Science Institute, which is operated by the Association of Universities for Research in Astronomy, Inc., under NASA contract NAS 5-03127 for JWST. These observations are associated with programme #1288 (DOI: 10.17909/pg4c-1737). Support for programme #1288 was provided by NASA through a grant from the Space Telescope Science Institute, which is operated by the Association of Universities for Research in Astronomy, Inc., under NASA contract NAS 5-03127. E.P. and J.C. acknowledge support from the University of Western Ontario, the Institute for Earth and Space Exploration, the Canadian Space Agency (CSA, 22JWGO1-16), and the Natural Sciences and Engineering Research Council of Canada. JRG and SC thank the Spanish MCINN for funding support under grant PID2019-106110GB-I00. C.B. is grateful for an appointment at NASA Ames Research Center through the San José State University Research Foundation (80NSSC22M0107). TO acknowledges support from JSPS Bilateral Program, Grant Number 120219939. MGW acknowledges partial support from JWST Theory grant JWST-AR-01557.001-A. EB, DL, RM, FLP and ER acknowledge support by the Programme National "Physique et Chimie du Milieu Interstellaire" (PCMI) of CNRS/INSU with INC/INP, co-funded by CEA and CNES. Work by YO and MR is carried out within the Collaborative Research Centre 956, sub-project C1, funded by the Deutsche Forschungsgemeinschaft (DFG) – project ID 184018867. I.A. is funded by a fellowship in the Program of Academic Research Projects Management, PRPI-USP. MB acknowledges DST, India for the DST INSPIRE Faculty fellowship. JH acknowledges support from the Chinese Academy of Sciences (CAS), through a grant to the CAS South America Center for Astronomy (CASSACA) in Santiago, Chile. MSK is funded by the Russian Science Foundation, grant 21-12-00373. P.M. acknowledges grants EUR2021-122006, TED2021-129416A-I00 and PID2021-125309OA-I00 funded by MCIN/AEI/ 10.13039/501100011033 and European Union NextGenerationEU/PRTR. NN is funded by the United Arab Emirates University (UAEU) through UAEU Program for Advanced Research (UPAR) grant G00003479. A.P. acknowledges financial assistance from the Banaras Hindu University's IoE grant (R/Dev/D/IoE/Incentive/2021- 22/32439) as well as funding from the SERB, New Delhi through Core Research Grant (CRG/2021/000907) and IUCAA, Pune for associateship. HZ acknowledges support from the Swedish Research Council (contract No 2020-03437).

Data availability: The following data products are provided via the CDS: (1) the five template spectra, (2) the complete version of Table 3 listing the intensities (observed and corrected for extinction using foreground and intermingled formalisms) and column densities of the H_2 lines in $v = 0$ and $v = 1$ states as observed in the five template, and (3) a table with all lines detected in the five template spectra, their identification and their surface brightness (see Appendix B). The following data products are provided via the PDRs4All high-level science products (HLSPs) collection on the Mikulski Archive for Space Telescopes (MAST; `https://mast.stsci.edu/`, DOI: `https://doi.org/10.17909/wqwy-p406`): (1) the NIRSpec cubes, (2) the extraction apertures for the five template spectra and the NIRSpec cut, (3) surface brightness maps of lines and AIBs and maps of physical parameters, (4) surface brightness cuts of lines and AIBs, cuts of physical parameters and the location of the cut, and (5) the reference line list (Sect. 4.2). All links to data products are referenced on the PDRs4All website (`https://pdrs4all.org`).

[31] `https://pdrs4all.org`

References

Abgrall, H., Le Bourlot, J., Pineau Des Forets, G., et al. 1992, A&A, 253, 525
Agúndez, M., Goicoechea, J. R., Cernicharo, J., Faure, A., & Roueff, E. 2010, ApJ, 713, 662
Allamandola, L. J., Tielens, A. G. G. M., & Barker, J. R. 1989, ApJS, 71, 733
Allamandola, L. J., Boersma, C., Lee, T. J., Bregman, J. D., & Temi, P. 2021, ApJ, 917, L35
Allers, K. N., Jaffe, D. T., Lacy, J. H., Draine, B. T., & Richter, M. J. 2005, ApJ, 630, 368
Andree-Labsch, S., Ossenkopf-Okada, V., & Röllig, M. 2017, A&A, 598, A2
Arab, H., Abergel, A., Habart, E., et al. 2012, A&A, 541, A19
Baldwin, J. A., Verner, E. M., Verner, D. A., et al. 2000, ApJS, 129, 229
Bally, J. 2008, in Handbook of Star Forming Regions, Volume I, 4, ed. B. Reipurth, 459
Bally, J., O'Dell, C. R., & McCaughrean, M. J. 2000, AJ, 119, 2919
Bernard-Salas, J., & Tielens, A. G. G. M. 2005, A&A, 431, 523
Bernard-Salas, J., Habart, E., Arab, H., et al. 2012, A&A, 538, A37
Berné, O., Habart, É., Peeters, E., et al. 2022, PASP, 134, 054301
Berné, O., Martin-Drumel, M.-A., Schroetter, I., et al. 2023, Nature, 621, 56
Berné, O., Habart, E., Peeters, E., et al. 2024, Science, 383, 988
Bertoldi, F., & Draine, B. T. 1996, ApJ, 458, 222
Black, J. H., & Dalgarno, A. 1976, ApJ, 203, 132
Blagrave, K. P. M., Martin, P. G., Rubin, R. H., et al. 2007, ApJ, 655, 299
Boersma, C., Rubin, R. H., & Allamandola, L. J. 2012, ApJ, 753, 168
Böker, T., Arribas, S., Lützgendorf, N., et al. 2022, A&A, 661, A82
Boogert, A. C. A., Gerakines, P. A., & Whittet, D. C. B. 2015, ARA&A, 53, 541
Bregman, J. D., Allamandola, L. J., Tielens, A. G. G. M., Geballe, T. R., & Witteborn, F. C. 1989, ApJ, 344, 791
Brieva, A. C., Gredel, R., Jäger, C., Huisken, F., & Henning, T. 2016, ApJ, 826, 122
Brooke, J. S. A., Bernath, P. F., Western, C. M., et al. 2016, J. Quant. Spec. Radiat. Transf., 168, 142
Buragohain, M., Pathak, A., Sarre, P., Onaka, T., & Sakon, I. 2015, MNRAS, 454, 193
Burton, M. G., Hollenbach, D. J., & Tielens, A. G. G. M. 1990, ApJ, 365, 620
Cardelli, J. A., Clayton, G. C., & Mathis, J. S. 1989, ApJ, 345, 245
Champion, J., Berné, O., Vicente, S., et al. 2017, A&A, 604, A69
Changala, P. B., Neufeld, D. A., & Godard, B. 2021, ApJ, 917, 16
Chown, R., Sidhu, A., Peeters, E., et al. 2024, A&A, 685, A75
Code, A. D. 1973, in Interstellar Dust and Related Topics, 52, eds. J. M. Greenberg, & H. C. van de Hulst, 505
Cuadrado, S., Goicoechea, J. R., Pilleri, P., et al. 2015, A&A, 575, A82
Cuadrado, S., Goicoechea, J. R., Cernicharo, J., et al. 2017, A&A, 603, A124
Cuadrado, S., Salas, P., Goicoechea, J. R., et al. 2019, A&A, 625, A3
Del Zanna, G., & Storey, P. J. 2022, MNRAS, 513, 1198
Doney, K. D., Candian, A., Mori, T., Onaka, T., & Tielens, A. G. G. M. 2016, A&A, 586, A65
Draine, B. T. 2011, Physics of the Interstellar and Intergalactic Medium (Princeton University Press)
Egorov, O. V., Lozinskaya, T. A., Moiseev, A. V., & Smirnov-Pinchukov, G. V. 2014, MNRAS, 444, 376
Egorov, O. V., Lozinskaya, T. A., Moiseev, A. V., & Shchekinov, Y. A. 2017, MNRAS, 464, 1833
Elliott, K. H., & Meaburn, J. 1974, Ap&SS, 28, 351

Elmegreen, B. G., & Lada, C. J. 1977, ApJ, 214, 725
Escalante, V., & Victor, G. A. 1990, ApJS, 73, 513
Esteban, C., Vilchez, J. M., & Smith, L. J. 1994, AJ, 107, 1041
Esteban, C., Peimbert, M., Torres-Peimbert, S., & Escalante, V. 1998, MNRAS, 295, 401
Ferland, G. J., Chatzikos, M., Guzmán, F., et al. 2017, Rev. Mex. Astron. Astrofis., 53, 385
Fuente, A., Rodriguez-Franco, A., Garcia-Burillo, S., Martin-Pintado, J., & Black, J. H. 2003, A&A, 406, 899
Gardner, J. P., Mather, J. C., Clampin, M., et al. 2006, Space Sci. Rev., 123, 485
Geballe, T. R., Tielens, A. G. G. M., Allamandola, L. J., Moorhouse, A., & Brand, P. W. J. L. 1989, ApJ, 341, 278
Genzel, R., & Stutzki, J. 1989, ARA&A, 27, 41
Gerin, M., Neufeld, D. A., & Goicoechea, J. R. 2016, ARA&A, 54, 181
Giard, M., Bernard, J. P., Lacombe, F., Normand, P., & Rouan, D. 1994, A&A, 291, 239
Gibb, E. L., Whittet, D. C. B., Boogert, A. C. A., & Tielens, A. G. G. M. 2004, ApJS, 151, 35
Godard, B., & Cernicharo, J. 2013, A&A, 550, A8
Goicoechea, J. R., & Roncero, O. 2022, A&A, 664, A190
Goicoechea, J. R., Teyssier, D., Etxaluze, M., et al. 2015, ApJ, 812, 75
Goicoechea, J. R., Pety, J., Cuadrado, S., et al. 2016, Nature, 537, 207
Goicoechea, J. R., Cuadrado, S., Pety, J., et al. 2017, A&A, 601, A9
Gordon, I. E., Rothman, L. S., Hargreaves, R. J., et al. 2022, J. Quant. Spec. Radiat. Transf., 277, 107949
Gordon, K. D., Clayton, G. C., Decleir, M., et al. 2023, ApJ, 950, 86
Gorti, U., & Hollenbach, D. 2002, ApJ, 573, 215
Großschedl, J. E., Alves, J., Meingast, S., et al. 2018, A&A, 619, A106
Guan, L., Jiang, P., Zhang, G., et al. 2021, A&A, 647, A127
Güdel, M., Briggs, K. R., Montmerle, T., et al. 2008, Science, 319, 309
Habart, E., Dartois, E., Abergel, A., et al. 2010, A&A, 518, A116
Habart, E., Le Gal, R., Alvarez, C., et al. 2023, A&A, 673, A149
Habart, E., Peeters, E., Berné, O., et al. 2024, A&A, 685, A73
Henney, W. J. 2021, MNRAS, 502, 4597
Henney, W. J., Williams, R. J. R., Ferland, G. J., Shaw, G., & O'Dell, C. R. 2007, ApJ, 671, L137
Herrmann, F., Madden, S. C., Nikola, T., et al. 1997, ApJ, 481, 343
Hillenbrand, L. A., & Carpenter, J. M. 2000, ApJ, 540, 236
Hogerheijde, M. R., Jansen, D. J., & van Dishoeck, E. F. 1995, A&A, 294, 792
Hopkins, P. F., Quataert, E., & Murray, N. 2012, MNRAS, 421, 3522
Hudgins, D. M., Bauschlicher, C. W., J., & Sandford, S. A. 2004, ApJ, 614, 770
Hummer, D. G., & Storey, P. J. 1987, MNRAS, 224, 801
Jakobsen, P., Ferruit, P., Alves de Oliveira, C., et al. 2022, A&A, 661, A80
Jansen, D. J., Spaans, M., Hogerheijde, M. R., & Van Dishoeck, E. F. 1995, A&A, 303, 541
Joblin, C., Tielens, A. G. G. M., Allamandola, L. J., & Geballe, T. R. 1996, ApJ, 458, 610
Joblin, C., Bron, E., Pinto, C., et al. 2018, A&A, 615, A129
Kaplan, K. F., Dinerstein, H. L., Oh, H., et al. 2017, ApJ, 838, 152
Kaplan, K. F., Dinerstein, H. L., Kim, H., & Jaffe, D. T. 2021, ApJ, 919, 27
Kim, C.-G., Ostriker, E. C., & Kim, W.-T. 2013, ApJ, 776, 1
Kirsanova, M. S., Sobolev, A. M., Thomasson, M., et al. 2008, MNRAS, 388, 729
Knight, C., Peeters, E., Stock, D. J., Vacca, W. D., & Tielens, A. G. G. M. 2021, ApJ, 918, 8
Knight, C., Peeters, E., Tielens, A. G. G. M., & Vacca, W. D. 2022, MNRAS, 509, 3523
Koenig, X. P., Allen, L. E., Gutermuth, R. A., et al. 2008, ApJ, 688, 1142
Kounkel, M., Covey, K., Suárez, G., et al. 2018, AJ, 156, 84
Kraemer, K. E., Engelke, C. W., Renger, B. A., & Sloan, G. C. 2022, AJ, 164, 161
Krasnobaev, K. V., & Tagirova, R. R. 2017, MNRAS, 469, 1403
Krasnobaev, K. V., Tagirova, R. R., Arafailov, S. I., & Kotova, G. Y. 2016, Astron. Lett., 42, 460
Lai, T. S. Y., Smith, J. D. T., Baba, S., Spoon, H. W. W., & Imanishi, M. 2020, ApJ, 905, 55
Le Bourlot, J., Pineau Des Forets, G., Roueff, E., & Flower, D. R. 1993, A&A, 267, 233
Le Petit, F., Nehmé, C., Le Bourlot, J., & Roueff, E. 2006, ApJS, 164, 506
Leurini, S., Rolffs, R., Thorwirth, S., et al. 2006, A&A, 454, L47
Lis, D. C., & Schilke, P. 2003, ApJ, 597, L145
Luhman, K. L., Engelbracht, C. W., & Luhman, M. L. 1998, ApJ, 499, 799
Luhman, M. L., Jaffe, D. T., Keller, L. D., & Pak, S. 1994, ApJ, 436, L185
Mackie, C. J., Candian, A., Huang, X., et al. 2015, J. Chem. Phys., 143, 224314
Mackie, C. J., Candian, A., Huang, X., et al. 2016, J. Chem. Phys., 145, 084313
Mackie, C. J., Candian, A., Lee, T. J., & Tielens, A. G. G. M. 2022, J. Phys. Chem. A, 126, 3198
Maltseva, E., Petrignani, A., Candian, A., et al. 2015, ApJ, 814, 23
Maltseva, E., Petrignani, A., Candian, A., et al. 2016, ApJ, 831, 58
Marconi, A., Testi, L., Natta, A., & Walmsley, C. M. 1998, A&A, 330, 696
Martín-Hernández, N. L., Bik, A., Kaper, L., Tielens, A. G. G. M., & Hanson, M. M. 2003, A&A, 405, 175
McLeod, A. F., Dale, J. E., Ginsburg, A., et al. 2015, MNRAS, 450, 1057
Méndez-Delgado, J. E., Henney, W. J., Esteban, C., et al. 2021, ApJ, 918, 27
Menten, K. M., Reid, M. J., Forbrich, J., & Brunthaler, A. 2007, A&A, 474, 515
Mori, T. I., Onaka, T., Sakon, I., et al. 2014, ApJ, 784, 53
Nagy, Z., Van der Tak, F. F. S., Ossenkopf, V., et al. 2013, A&A, 550, A96
Neufeld, D. A., Godard, B., Bryan Changala, P., et al. 2021, ApJ, 917, 15
O'Dell, C. R. 2001, ARA&A, 39, 99
O'Dell, C. R., Kollatschny, W., & Ferland, G. J. 2017, ApJ, 837, 151
O'Dell, C. R., Abel, N. P., & Ferland, G. J. 2020, ApJ, 891, 46
Ojha, D. K., Samal, M. R., Pandey, A. K., et al. 2011, ApJ, 738, 156
Onaka, T., Mori, T. I., Sakon, I., et al. 2014, ApJ, 780, 114
Onaka, T., Sakon, I., & Shimonishi, T. 2022, ApJ, 941, 190
Ossenkopf, V., Röllig, M., Neufeld, D. A., et al. 2013, A&A, 550, A57
Osterbrock, D. E., Tran, H. D., & Veilleux, S. 1992, ApJ, 389, 305
Pabst, C., Higgins, R., Goicoechea, J. R., et al. 2019, Nature, 565, 618
Pabst, C. H. M., Goicoechea, J. R., Teyssier, D., et al. 2020, A&A, 639, A2
Parikka, A., Habart, E., Bernard-Salas, J., Köhler, M., & Abergel, A. 2018, A&A, 617, A77
Parmar, P. S., Lacy, J. H., & Achtermann, J. M. 1991, ApJ, 372, L25
Peeters, E., Allamandola, L. J., Bauschlicher, C. W., J., et al. 2004, ApJ, 604, 252
Peeters, E., Tielens, A. G. G. M., Allamandola, L. J., & Wolfire, M. G. 2012, ApJ, 747, 44
Peeters, E., Bauschlicher, Jr., C. W., Allamandola, L. J., et al. 2017, ApJ, 836, 198
Pellegrini, E. W., Baldwin, J. A., Ferland, G. J., Shaw, G., & Heathcote, S. 2009, ApJ, 693, 285
Pilleri, P., Montillaud, J., Berné, O., & Joblin, C. 2012, A&A, 542, A69
Pilleri, P., Joblin, C., Boulanger, F., & Onaka, T. 2015, A&A, 577, A16
Pound, M. W., & Wolfire, M. G. 2023, AJ, 165, 25
Preibisch, T. & Zinnecker, H. 1999, AJ, 117, 2381
Prozesky, A., & Smits, D. P. 2018, MNRAS, 478, 2766
Reiter, M., McLeod, A. F., Klaassen, P. D., et al. 2019, MNRAS, 490, 2056
Riashchikov, D. S., Pomelnikov, I. A., & Molevich, N. E. 2022, Bull. Lebedev Phys. Inst., 49, 307
Röllig, M., Abel, N. P., Bell, T., et al. 2007, A&A, 467, 187
Roueff, E., Abgrall, H., Czachorowski, P., et al. 2019, A&A, 630, A58
Rubin, R. H., Simpson, J. P., O'Dell, C. R., et al. 2011, MNRAS, 1526
Salas, P., Oonk, J. B. R., Emig, K. L., et al. 2019, A&A, 626, A70
Salgado, F., Berné, O., Adams, J. D., et al. 2016, ApJ, 830, 118
Schirmer, T., Ysard, N., Habart, E., et al. 2022, A&A, 666, A49
Sellgren, K. 1984, ApJ, 277, 623
Sellgren, K., Tokunaga, A. T., & Nakada, Y. 1990, ApJ, 349, 120
Shaw, G., Ferland, G. J., Henney, W. J., et al. 2009, ApJ, 701, 677
Sheffer, Y., Wolfire, M. G., Hollenbach, D. J., Kaufman, M. J., & Cordier, M. 2011, ApJ, 741, 45
Simon, R., Stutzki, J., Sternberg, A., & Winnewisser, G. 1997, A&A, 327, L9
Sloan, G. C., Bregman, J. D., Geballe, T. R., Allamandola, L. J., & Woodward, E. 1997, ApJ, 474, 735
Smith, J. D. T., Draine, B. T., Dale, D. A., et al. 2007, ApJ, 656, 770
Smits, D. P. 1996, MNRAS, 278, 683
Sota, A., Maíz Apellániz, J., Walborn, N. R., et al. 2011, ApJS, 193, 24
Stacey, G. J., Jaffe, D. T., Geis, N., et al. 1993, ApJ, 404, 219
Sternberg, A., & Dalgarno, A. 1989, ApJ, 338, 197
Sternberg, A., & Dalgarno, A. 1995, ApJS, 99, 565
Stock, D. J., & Peeters, E. 2017, ApJ, 837, 129
Stoerzer, H., Stutzki, J., & Sternberg, A. 1995, A&A, 296, L9
Störzer, H., & Hollenbach, D. 1998, ApJ, 495, 853
Tabone, B., van Hemert, M. C., van Dishoeck, E. F., & Black, J. H. 2021, A&A, 650, A192
Tauber, J. A., Tielens, A. G. G. M., Meixner, M., & Goldsmith, P. F. 1994, ApJ, 422, 136
Tauber, J. A., Lis, D. C., Keene, J., Schilke, P., & Buettgenbach, T. H. 1995, A&A, 297, 567
Tielens, A. 2005, The Physics and Chemistry of the Interstellar Medium (Springer Netherlands)
Tielens, A. G. 2021, Molecular Astrophysics (Cambridge University Press)
Tielens, A. G. G. M., & Hollenbach, D. 1985a, ApJ, 291, 722
Tielens, A. G. G. M., & Hollenbach, D. 1985b, ApJ, 291, 747
Tielens, A. G. G. M., Meixner, M. M., van der Werf, P. P., et al. 1993, Science, 262, 86
Van De Putte, D., Meshaka, R., Trahin, B., et al. 2024, A&A, accepted [arXiv:2404.03111]

van der Tak, F. F. S., Nagy, Z., Ossenkopf, V., et al. 2013, A&A, 560, A95
van der Werf, P. P., Stutzki, J., Sternberg, A., & Krabbe, A. 1996, A&A, 313, 633
van der Werf, P. P., Goss, W. M., & O'Dell, C. R. 2013, ApJ, 762, 101
van der Wiel, M. H. D., van der Tak, F. F. S., Ossenkopf, V., et al. 2009, A&A, 498, 161
van Diedenhoven, B., Peeters, E., Van Kerckhoven, C., et al. 2004, ApJ, 611, 928
van Dishoeck, E. F., & Black, J. H. 1988, ApJ, 334, 771
van Hoof, P. A. M. 2018, Galaxies, 6, 63
Vicente, S., Berné, O., Tielens, A., et al. 2013, ApJ, 765, L38
Visser, R., van Dishoeck, E. F., & Black, J. H. 2009, A&A, 503, 323
Walmsley, C. M., Natta, A., Oliva, E., & Testi, L. 2000, A&A, 364, 301
Weilbacher, P. M., Monreal-Ibero, A., Kollatschny, W., et al. 2015, A&A, 582, A114
Wen, Z., & O'dell, C. 1995, ApJ, 438, 784
Wiersma, S. D., Candian, A., Bakker, J. M., et al. 2020, A&A, 635, A9
Williams, J. P., & McKee, C. F. 1997, ApJ, 476, 166
Wolfire, M. G., McKee, C. F., Hollenbach, D., & Tielens, A. G. G. M. 2003, ApJ, 587, 278
Wolfire, M. G., Hollenbach, D., & McKee, C. F. 2010, ApJ, 716, 1191
Wolfire, M. G., Vallini, L., & Chevance, M. 2022, ARA&A, 60, 247
Wyrowski, F., Schilke, P., Hofner, P., & Walmsley, C. M. 1997, ApJ, 487, L171
Yang, X. J., Li, A., & Glaser, R. 2020, ApJS, 251, 12
Yang, X. J., Li, A., He, C. Y., & Glaser, R. 2021, ApJS, 255, 23
Young Owl, R. C., Meixner, M. M., Wolfire, M., Tielens, A. G. G. M., & Tauber, J. 2000, ApJ, 540, 886
Yousefi, M., Bernath, P. F., Hodges, J., & Masseron, T. 2018, J. Quant. Spec. Radiat. Transf., 217, 416
Zannese, M., Tabone, B., Habart, E., et al. 2023, A&A, 671, A41
Zannese, M., Tabone, B., Habart, E., et al. 2024, Nat. Astron., in press https://doi.org/10.1038/s41550-024-02203-0
Zatsarinny, O., & Bartschat, K. 2013, J. Phys. B At. Mol. Phys., 46, 112001
Zatsarinny, O., Bartschat, K., Bandurina, L., & Gedeon, V. 2005, Phys. Rev. A, 71, 042702

[1] Department of Physics & Astronomy, The University of Western Ontario, London ON N6A 3K7, Canada
e-mail: pis@pdrs4all.org
[2] Institute for Earth and Space Exploration, The University of Western Ontario, London ON N6A 3K7, Canada
[3] Carl Sagan Center, SETI Institute, 339 Bernardo Avenue, Suite 200, Mountain View, CA 94043, USA
[4] Institut d'Astrophysique Spatiale, Université Paris-Saclay, CNRS, Bâtiment 121, 91405 Orsay Cedex, France
[5] Institut de Recherche en Astrophysique et Planétologie, Université Toulouse III – Paul Sabatier, CNRS, CNES, 9 Av. du colonel Roche, 31028 Toulouse Cedex 04, France
[6] Space Telescope Science Institute, 3700 San Martin Drive, Baltimore, MD 21218, USA
[7] Department of Astronomy, University of Michigan, 1085 South University Avenue, Ann Arbor, MI 48109, USA
[8] Leiden Observatory, Leiden University, PO Box 9513, 2300 RA Leiden, The Netherlands
[9] Astronomy Department, University of Maryland, College Park, MD 20742, USA
[10] Institut des Sciences Moléculaires d'Orsay, Université Paris-Saclay, CNRS, Bâtiment 520, 91405 Orsay Cedex, France
[11] Instituto de Física Fundamental (CSIC), Calle Serrano 121-123, 28006, Madrid, Spain
[12] NASA Ames Research Center, MS 245-6, Moffett Field, CA 94035-1000, USA
[13] Department of Astronomy, Graduate School of Science, The University of Tokyo, 7-3-1 Bunkyo-ku, Tokyo 113-0033, Japan
[14] Department of Physics, Faculty of Science and Engineering, Meisei University, 2-1-1 Hodokubo, Hino, Tokyo 191-8506, Japan
[15] Instituto de Astrofísica e Ciências do Espaço, Tapada da Ajuda, Edifício Leste, 2° Piso, 1349-018 Lisboa, Portugal
[16] ACRI-ST, Centre d'Etudes et de Recherche de Grasse (CERGA), 10 Av. Nicolas Copernic, 06130 Grasse, France
[17] INCLASS Common Laboratory, 10 Av. Nicolas Copernic, 06130 Grasse, France
[18] LERMA, Observatoire de Paris, PSL Research University, CNRS, Sorbonne Universités, 92190 Meudon, France
[19] UK Astronomy Technology Centre, Royal Observatory Edinburgh, Blackford Hill EH9 3HJ, UK
[20] Observatorio Astronómico Nacional (OAN,IGN), Alfonso XII, 3, 28014 Madrid, Spain
[21] Sterrenkundig Observatorium, Universiteit Gent, Gent, Belgium
[22] Quantum Solid State Physics (QSP), Celestijnenlaan 200d – Box 2414, 3001 Leuven, Belgium
[23] Institut de Planétologie et d'Astrophysique de Grenoble (IPAG), Université Grenoble Alpes, CNRS, 38000 Grenoble, France
[24] Institut de Radioastronomie Millimétrique (IRAM), 300 Rue de la Piscine, 38406 Saint-Martin d'Hères, France
[25] I. Physikalisches Institut der Universität zu Köln, Zülpicher Straße 77, 50937 Köln, Germany
[26] Johns Hopkins University, 3400 N. Charles Street, Baltimore, MD, 21218, USA
[27] Physikalischer Verein – Gesellschaft für Bildung und Wissenschaft, Robert-Mayer-Str. 2, 60325 Frankfurt, Germany
[28] Goethe-Universität, Physikalisches Institut, Frankfurt am Main, Germany
[29] Department of Space, Earth and Environment, Chalmers University of Technology, Onsala Space Observatory, 439 92 Onsala, Sweden
[30] Instituto de Física e Química, Universidade Federal de Itajubá, Av. BPS 1303, Pinheirinho, 37500-903, Itajubá, MG, Brazil
[31] Institute of Mathematics and Statistics, University of São Paulo, Rua do Matão, 1010, Cidade Universitária, Butantã, 05508-090 São Paulo, SP, Brazil
[32] Instituto de Física e Química, Universidade Federal de Itajubá, Av. BPS 1303, Pinheirinho, 37500-903 Itajubá, MG, Brazil
[33] Bay Area Environmental Research Institute, Moffett Field, CA 94035, USA
[34] Australian Synchrotron, Australian Nuclear Science and Technology Organisation (ANSTO), Victoria, Australia
[35] INAF – Osservatorio Astrofisico di Catania, Via Santa Sofia 78, 95123 Catania, Italy
[36] Laboratoire de Physique de l'École Normale Supérieure, ENS, Université PSL, CNRS, Sorbonne Université, Université de Paris, 75005 Paris, France
[37] Laboratory for Atmospheric and Space Physics, University of Colorado, Boulder, CO 80303, USA
[38] Department of Chemistry, University of Colorado, Boulder, CO 80309, USA
[39] Institute for Modeling Plasma, Atmospheres, and Cosmic Dust (IMPACT), University of Colorado, Boulder, CO 80303, USA
[40] Faculty of Aerospace Engineering, Delft University of Technology, Kluyverweg 1, 2629 HS Delft, The Netherlands
[41] Radboud University, Institute for Molecules and Materials, FELIX Laboratory, Toernooiveld 7, 6525 ED Nijmegen, The Netherlands
[42] School of Physics, University of Hyderabad, Hyderabad, Telangana 500046, India
[43] Department of Physics, Wellesley College, 106 Central Street, Wellesley, MA 02481, USA
[44] Anton Pannekoek Institute for Astronomy, University of Amsterdam, The Netherlands
[45] Delft University of Technology, Delft, The Netherlands
[46] Laboratoire de Physique des deux infinis Irène Joliot-Curie, Université Paris-Saclay, CNRS/IN2P3, Bâtiment 104, 91405 Orsay Cedex, France
[47] Department of Chemistry, GITAM school of Science, GITAM Deemed to be University, Bangalore, India
[48] Institut de Physique de Rennes, UMR CNRS 6251, Université de Rennes 1, Campus de Beaulieu, 35042 Rennes Cedex, France
[49] Department of Chemistry, The University of British Columbia, Vancouver, British Columbia, Canada
[50] National Radio Astronomy Observatory (NRAO), 520 Edgemont Road, Charlottesville, VA 22903, USA
[51] European Space Astronomy Centre (ESAC/ESA), Villanueva de la Cañada, 28692 Madrid, Spain
[52] Observatoire de Paris, PSL University, Sorbonne Université, LERMA, CNRS, 75014, Paris, France

[53] Harvard-Smithsonian Center for Astrophysics, 60 Garden Street, Cambridge, MA 02138, USA
[54] Sorbonne Université, CNRS, UMR 7095, Institut d'Astrophysique de Paris, 98bis bd Arago, 75014 Paris, France
[55] Institut Universitaire de France, Ministère de l'Enseignement Supérieur et de la Recherche, 1 rue Descartes, 75231 Paris Cedex 05, France
[56] Department of Physics and Astronomy, Rice University, Houston, TX 77005-1892, USA
[57] Yunnan Observatories, Chinese Academy of Sciences, 396 Yangfangwang, Guandu District, Kunming, 650216, PR China
[58] Chinese Academy of Sciences South America Center for Astronomy, National Astronomical Observatories, CAS, Beijing 100101, PR China
[59] Departments of Chemistry and Astronomy, University of Virginia, Charlottesville, VA 22904, USA
[60] InterCat and Dept. Physics and Astron., Aarhus University, Ny Munkegade 120, 8000 Aarhus C, Denmark
[61] Laboratory Astrophysics Group of the Max Planck Institute for Astronomy at the Friedrich Schiller University Jena, Institute of Solid State Physics, Helmholtzweg 3, 07743 Jena, Germany
[62] Instituto de Astronomia, Geofísica e Ciências Atmosféricas, Universidade de São Paulo, 05509-090 São Paulo, SP, Brazil
[63] Department of Physics and Astronomy, San José State University, San Jose, CA 95192, USA
[64] European Space Agency, Space Telescope Science Institute, 3700 San Martin Drive, Baltimore, MD 21218, USA
[65] Institute of Astronomy, Russian Academy of Sciences, 119017, Pyatnitskaya str., 48 , Moscow, Russia
[66] Department of Earth, Ocean, & Atmospheric Sciences, University of British Columbia, British Columbia V6T 1Z4, Canada
[67] Telespazio UK for ESA, ESAC, 28692 Villanueva de la Cañada, Madrid, Spain
[68] IPAC, California Institute of Technology, Pasadena, CA, USA
[69] LAB, Université de Bordeaux, CNRS, B18N, 33615 Pessac, France
[70] Department of Physics and Astronomy, University of Missouri, Columbia, MO 65211, USA
[71] Max Planck Institute for Astronomy, Königstuhl 17, 69117 Heidelberg, Germany
[72] Chemical Sciences Division, Lawrence Berkeley National Laboratory, Berkeley, CA, USA
[73] Kenneth S. Pitzer Center for Theoretical Chemistry, Department of Chemistry, University of California – Berkeley, Berkeley, CA, USA
[74] AIM, CEA, CNRS, Université Paris-Saclay, Université Paris Diderot, Sorbonne Paris Cité, 91191 Gif-sur-Yvette, France
[75] Institut des Sciences Moléculaires, CNRS, Université de Bordeaux, 33405 Talence, France
[76] Department of Chemistry, Massachusetts Institute of Technology, Cambridge, MA 02139, USA
[77] Instituto de Ciencia de Materiales de Madrid (CSIC), Sor Juana Ines de la Cruz 3, 28049 Madrid, Spain
[78] Department of Physics, PO Box 64, 00014 University of Helsinki, Finland
[79] Steward Observatory, University of Arizona, Tucson, AZ 85721-0065, USA
[80] AstronetX PBC, 55 Post Rd W FL 2, Westport, CT 06880, USA
[81] Department of Physics, College of Science, United Arab Emirates University (UAEU), Al-Ain 15551, UAE
[82] National Astronomical Observatory of Japan, National Institutes of Natural Science, 2-21-1 Osawa, Mitaka, Tokyo 181-8588, Japan
[83] Department of Physics, Institute of Science, Banaras Hindu University, Varanasi 221005, India
[84] University of Central Florida, Orlando, FL 32765, USA
[85] Van't Hoff Institute for Molecular Sciences, University of Amsterdam, PO Box 94157, 1090 GD Amsterdam, The Netherlands
[86] Laboratoire de Chimie et Physique Quantiques LCPQ/IRSAMC, UMR5626, Université de Toulouse (UPS) and CNRS, Toulouse, France
[87] Instituto de Matemática, Estatística e Física, Universidade Federal do Rio Grande, 96201-900 Rio Grande, RS, Brazil
[88] Center for Astrophysics and Space Sciences, Department of Physics, University of California, San Diego, 9500 Gilman Drive, La Jolla, CA 92093, USA
[89] School of Chemistry, The University of Nottingham, University Park, Nottingham NG7 2RD, UK
[90] Astronomy Department, Ohio State University, Columbus, OH 43210, USA
[91] Space Science Institute, 4765 Walnut St., R203, Boulder, CO 80301, USA
[92] Department of Physics, Stockholm University, 10691 Stockholm, Sweden
[93] Department of Physics, Texas State University, San Marcos, TX 78666, USA
[94] Ritter Astrophysical Research Center, University of Toledo, Toledo, OH 43606, USA
[95] School of Physics and Astronomy, Sun Yat-sen University, 2 Da Xue Road, Tangjia, Zhuhai 519000, Guangdong Province, PR China
[96] Star and Planet Formation Laboratory, 0–0 S(RIKEN Cluster for Pioneering Research, Hirosawa 2-1, Wako, Saitama 351-0198, Japan
[97] Institute of Deep Space Sciences, Deep Space Exploration Laboratory, Hefei 230026, PR China
[98] Departamento de Astronomía, Universidad de Chile, Las Condes, 7591245 Santiago, Chile
[99] INAF – Osservatorio Astronomico di Cagliari, via della Scienza 5, 09047 Selargius (CA), Italy